$|V_{ub}|$ from $B \to \pi \ell \nu$ decays and $(2+1)$-flavor lattice QCD

Jon. A. Bailey,[1] A. Bazavov,[2,*] C. Bernard,[3] C. M. Bouchard,[4,5] C. DeTar,[6] D. Du,[7,8,†] A. X. El-Khadra,[7] J. Foley,[6]
E. D. Freeland,[9] E. Gámiz,[10] Steven Gottlieb,[11] U. M. Heller,[12] J. Komijani,[3] A. S. Kronfeld,[13,14] J. Laiho,[8] L. Levkova,[6]
Yuzhi Liu,[15] P. B. Mackenzie,[13] Y. Meurice,[16] E. Neil,[15,17] Si-Wei Qiu,[6,‡] J. N. Simone,[13] R. Sugar,[18] D. Toussaint,[19]
R. S. Van de Water,[13] and R. Zhou[13]

(Fermilab Lattice and MILC collaborations)

[1]Department of Physics and Astronomy, Seoul National University, Seoul, South Korea
[2]Physics Department, Brookhaven National Laboratory, Upton, New York, USA
[3]Department of Physics, Washington University, St. Louis, Missouri, USA
[4]Department of Physics, The Ohio State University, Columbus, Ohio, USA
[5]Physics Department, College of William and Mary, Williamsburg, Virginia, USA
[6]Department of Physics and Astronomy, University of Utah, Salt Lake City, Utah, USA
[7]Department of Physics, University of Illinois, Urbana, Illinois, USA
[8]Department of Physics, Syracuse University, Syracuse, New York, USA
[9]Liberal Arts Department, School of the Art Institute of Chicago, Chicago, Illinois, USA
[10]CAFPE and Departamento de Fisica Teórica y del Cosmos, Universidad de Granada, Granada, Spain
[11]Department of Physics, Indiana University, Bloomington, Indiana, USA
[12]American Physical Society, Ridge, New York, USA
[13]Fermi National Accelerator Laboratory, Batavia, Illinois, USA
[14]Institute for Advanced Study, Technische Universität München, Garching, Germany
[15]Department of Physics, University of Colorado, Boulder, Colorado, USA
[16]Department of Physics and Astronomy, University of Iowa, Iowa City, Iowa, USA
[17]RIKEN-BNL Research Center, Brookhaven National Laboratory, Upton, New York, USA
[18]Department of Physics, University of California, Santa Barbara, California, USA
[19]Physics Department, University of Arizona, Tucson, Arizona, USA

We present a lattice-QCD calculation of the $B \to \pi \ell \nu$ semileptonic form factors and a new determination of the CKM matrix element $|V_{ub}|$. We use the MILC asqtad $(2+1)$-flavor lattice configurations at four lattice spacings and light-quark masses down to $1/20$ of the physical strange-quark mass. We extrapolate the lattice form factors to the continuum using staggered chiral perturbation theory in the hard-pion and SU (2) limits. We employ a model-independent z parametrization to extrapolate our lattice form factors from large-recoil momentum to the full kinematic range. We introduce a new functional method to propagate information from the chiral-continuum extrapolation to the z expansion. We present our results together with a complete systematic error budget, including a covariance matrix to enable the combination of our form factors with other lattice-QCD and experimental results. To obtain $|V_{ub}|$, we simultaneously fit the experimental data for the $B \to \pi \ell \nu$ differential decay rate obtained by the BABAR and Belle collaborations together with our lattice form-factor results. We find $|V_{ub}| = (3.72 \pm 0.16) \times 10^{-3}$, where the error is from the combined fit to lattice plus experiments and includes all sources of uncertainty. Our form-factor results bring the QCD error on $|V_{ub}|$ to the same level as the experimental error. We also provide results for the $B \to \pi \ell \nu$ vector and scalar form factors obtained from the combined lattice and experiment fit, which are more precisely determined than from our lattice-QCD calculation alone. These results can be used in other phenomenological applications and to test other approaches to QCD.

I. INTRODUCTION

The Cabibbo-Kobayashi-Masakawa (CKM) matrix [1,2] element $|V_{ub}|$ is one of the fundamental parameters of the Standard Model and is an important input to searches for CP violation beyond the Standard Model. Constraints on new physics in the flavor sector are commonly cast in terms of overconstraining the apex of the CKM unitarity triangle. In contrast to the well-determined angle β of the unitarity

*Present address: Department of Physics and Astronomy, University of Iowa, Iowa City, Iowa, USA.
†dadu@syr.edu
‡Present address: Laboratory of Biological Modeling, NIDDK, NIH, Bethesda, Maryland, USA.

triangle, the opposite side $|V_{ub}/V_{cb}|$ is poorly determined, and the uncertainty is currently dominated by $|V_{ub}|$. This is due to the fact that charmless decays of the B meson have far smaller branching fractions than the charmed decays, as well as the fact that the theoretical calculations are less precise than for $\sin 2\beta$, $|V_{us}|$, or $|V_{cb}|$. Currently the most precise determination of $|V_{ub}|$ is obtained from charmless semileptonic B decays, using exclusive or inclusive methods that rely on the measurements of the branching fractions and the corresponding theoretical inputs. Exclusive determinations require knowledge of the form factors, while inclusive determinations rely on the operator product expansion, perturbative QCD, and nonperturbative input from experiments. There is a longstanding discrepancy between $|V_{ub}|$ determined from inclusive and exclusive decays: the central values from these two approaches differ by about 3σ. It was argued in Ref. [3] that this tension is unlikely to be due to new physics effects, and it is therefore important to examine the (theoretical and experimental) inputs to the $|V_{ub}|$ determinations. With the result obtained in this paper, the tension is reduced to 2.4σ.

In the limit of vanishing lepton mass, the Standard Model prediction for the differential decay rate of the exclusive semileptonic $B \rightarrow \pi\ell\nu$ decay is given by

$$\frac{d\Gamma(B \rightarrow \pi\ell\nu)}{dq^2} = \frac{G_F^2|V_{ub}|^2}{24\pi^3}|\boldsymbol{p}_\pi|^3|f_+(q^2)|^2, \quad (1.1)$$

where $|\boldsymbol{p}_\pi| = \frac{1}{2M_B}[(M_B^2 + M_\pi^2 - q^2)^2 - 4M_B^2M_\pi^2]^{1/2}$ is the pion momentum in the B-meson rest frame. To determine $|V_{ub}|$, the form factor $|f_+(q^2)|$ must be calculated with nonperturbative methods. The first unquenched lattice calculations of $|f_+(q^2)|$ with $2 + 1$ dynamical sea quarks were performed by HPQCD [4] and the Fermilab/MILC collaborations [5] several years ago. Here we extend and improve Ref. [5] in several ways.

The most recent exclusive determination of $|V_{ub}|$ from the Heavy Flavor Averaging Group (HFAG) [6] is based on combined lattice plus experiment fits and yields $|V_{ub}| = (3.28 \pm 0.29) \times 10^{-3}$, where the error includes both the experimental and theoretical uncertainties. The experimental data included in the average are the *BABAR* untagged six-q^2-bin data [7], the *BABAR* untagged twelve-q^2-bin data [8], the Belle untagged data [9], and the Belle hadronic tagged [10] data. The theoretical errors on the form factors from lattice QCD [5] are currently the dominant source of uncertainty in $|V_{ub}|$ [11]. Hence, a new lattice calculation of $f_+(q^2)$ with improved statistical and systematic errors is desirable.[1] To compare, the value of $|V_{ub}|$ from the inclusive method quoted by HFAG is about $(4.40 \pm 0.20) \times 10^{-3}$ [6] using the theory of Ref. [15].

In this paper, we present a new lattice-QCD calculation of the $B \rightarrow \pi\ell\nu$ semileptonic form factors and a determination of $|V_{ub}|$. Our calculation shares some features with the previous Fermilab/MILC calculation [5] but makes several improvements. We quadruple the statistics on the previously used ensembles and improve our strategy for extracting the form factors by including excited states in our three-point correlator analysis. In addition, we include twice as many ensembles in this analysis. The new ensembles have smaller lattice spacings, with the smallest lattice spacing decreased by half. This analysis also includes ensembles with light sea-quark masses that are much closer to their physical values ($m_l/m_s = 0.05$ versus 0.1). The smaller lattice spacings and light-quark masses provide much better control over the dominant systematic error due to the chiral-continuum extrapolation. We find that heavy-meson rooted staggered chiral perturbation theory (HMrSχPT) in the SU(2) and hard-pion limits provides a satisfactory description of our data. All together, these improvements reduce the error on the form factors by a factor of about 3. Finally, we introduce a new functional method for the extrapolation over the full kinematic range.

The determination of $|V_{ub}|$ from a combined fit to our lattice form factors together with experimental measurements also yields a very precise determination of the vector and scalar form factors over the entire kinematic range. These form factors will be valuable input to other phenomenological applications in the Standard Model and beyond. An example is the rare decay $B \rightarrow \pi\ell^+\ell^-$, which we will discuss in a separate paper.

Because our primary goal in this work was a reliable and precise determination of $|V_{ub}|$, we employed a blinding procedure to minimize subjective bias. At the stage of matching between the lattice and continuum vector currents, a slight multiplicative offset was applied to the data that was only known to two of the authors. The numerical value of the blinding factor was only disclosed after the analysis and error-estimation procedure, including the determination of $|V_{ub}|$, were essentially finalized.

This paper is organized as follows: In Sec. II, we present our calculation of the form factors. We describe the lattice actions, currents, simulation parameters, correlation functions, and fits to extract the matrix elements, renormalization of the currents, and adjustment of the form factors to correct for quark-mass mistunings. In Sec. III, we present the combined chiral-continuum extrapolation, followed by an itemized presentation of our complete error budget in Sec. IV. We then extrapolate the form factors to the full q^2 range through the functional z expansion method in Sec. V. We also perform fits to lattice and experimental data simultaneously to obtain $|V_{ub}|$. We conclude with a comparison to other results and discussion of the future outlook in Sec. VI. Preliminary reports of this work can be found in Refs. [16,17].

---

[1]Note that there are several other efforts with 2 [12] and $2 + 1$ flavors of sea quarks [13,14].

II. LATTICE-QCD SIMULATION

In this section, we describe the details of the lattice simulation. We briefly describe the calculation of the form factors in Sec. II A. We also calculate the tensor form factor, which follows an analysis similar to that of the vector and scalar form factors. The tensor form factor enters the Standard Model rate for $B \to \pi\ell^+\ell^-$ decay, and our final result for f_T will be presented in a forthcoming paper. In Sec. II B, we introduce the actions and simulation parameters used in this analysis. This is followed, in Sec. II C, by a brief discussion of the currents and lattice correlation functions. The correlator fits to extract the lattice form factors are provided in Sec. II D. In Sec. II E, we discuss the renormalization of the lattice currents. In Sec. II F, we correct the form factors *a posteriori* to account for the mistuning of the simulated heavy b-quark mass.

A. Form-factor definitions

The vector and tensor hadronic matrix elements relevant for $B \to \pi$ semileptonic decays can be parametrized by the following three form factors:

$$\langle\pi(p_\pi)|V^\mu|B(p_B)\rangle = \left(p_B^\mu + p_\pi^\mu - \frac{M_B^2 - M_\pi^2}{q^2}q^\mu\right)f_+(q^2)$$
$$+ \frac{M_B^2 - M_\pi^2}{q^2}q^\mu f_0(q^2), \qquad (2.1)$$

$$\langle\pi(p_\pi)|T^{\mu\nu}|B(p_B)\rangle = \frac{2}{M_B + M_\pi}(p_B^\mu p_\pi^\nu - p_B^\nu p_\pi^\mu)f_T(q^2), \qquad (2.2)$$

where $\mathcal{V}^\mu = \bar{q}\gamma^\mu b$, and $\mathcal{T}^{\mu\nu} = i\bar{q}\sigma^{\mu\nu}b$. In lattice gauge theory and in chiral perturbation theory, it is convenient to parametrize the vector-current matrix elements by [18]

$$\langle\pi(p_\pi)|V^\mu|B(p_B)\rangle = \sqrt{2M_B}[v^\mu f_\parallel(E_\pi) + p_{\pi,\perp}^\mu f_\perp(E_\pi)], \qquad (2.3)$$

where $v^\mu = p_B^\mu/M_B$ is the four-velocity of the B meson and $p_{\pi,\perp}^\mu = p_\pi^\mu - (p_\pi \cdot v)v^\mu$ is the projection of the pion momentum in the direction perpendicular to v^μ. The pion energy is related to the lepton momentum transfer q^2 by $E_\pi = p_\pi \cdot v = (M_B^2 + M_\pi^2 - q^2)/(2M_B)$. With this setup, we have

$$f_\parallel(E_\pi) = \frac{\langle\pi(p_\pi)|\mathcal{V}^4|B(p_B)\rangle}{\sqrt{2M_B}}, \qquad (2.4)$$

$$f_\perp(E_\pi) = \frac{\langle\pi(p_\pi)|\mathcal{V}^i|B(p_B)\rangle}{\sqrt{2M_B}}\frac{1}{p_\pi^i}, \qquad (2.5)$$

$$f_T(q^2) = \frac{M_B + M_\pi}{\sqrt{2M_B}}\frac{\langle\pi(p_\pi)|\mathcal{T}^{4i}|B(p_B)\rangle}{\sqrt{2M_B}}\frac{1}{p_\pi^i}, \qquad (2.6)$$

where no summation is implied by the repeated indices here. The form factors f_+ and f_0 are

$$f_+(q^2) = \frac{1}{\sqrt{2M_B}}[f_\parallel + (M_B - E_\pi)f_\perp], \qquad (2.7)$$

$$f_0(q^2) = \frac{\sqrt{2M_B}}{M_B^2 - M_\pi^2}[(M_B - E_\pi)f_\parallel + (E_\pi^2 - M_\pi^2)f_\perp]. \qquad (2.8)$$

B. Actions and parameters

The lattice gauge-field configurations we use have been generated by the MILC Collaboration [19–21], and some of their properties are listed in Table I. These twelve

TABLE I. Parameters of the MILC asqtad gauge-field ensembles used in this analysis. From left to right: Approximate lattice spacing a in fm, the (light/strange)-quark mass ratio am'_l/am'_h, the coupling constant β, the tadpole parameter u_0 determined from the plaquette, lattice volume, the number of configurations N_{cfg}, $M_\pi L$ (L is the spatial length of the lattice), and the number of configurations of the four ensembles that were used in Ref. [5].

| $\approx a$ (fm)	am'_l/am'_h	β	u_0	Volume	N_{cfg}	$M_\pi L$	N_{cfg} (Ref. [5])
0.12	0.01/0.05	6.760	0.8677	$20^3 \times 64$	2259	4.5	592
	0.007/0.05	6.760	0.8678	$20^3 \times 64$	2110	3.8	836
	0.005/0.05	6.760	0.8678	$24^3 \times 64$	2099	3.8	529
0.09	0.0062/0.031	7.090	0.8782	$28^3 \times 96$	1931	4.1	557
	0.00465/0.031	7.085	0.8781	$32^3 \times 96$	984	4.1	
	0.0031/0.031	7.080	0.8779	$40^3 \times 96$	1015	4.2	
	0.00155/0.031	7.075	0.877805	$64^3 \times 96$	791	4.8	
0.06	0.0072/0.018	7.480	0.8881	$48^3 \times 144$	593	6.3	
	0.0036/0.018	7.470	0.88788	$48^3 \times 144$	673	4.5	
	0.0025/0.018	7.465	0.88776	$56^3 \times 144$	801	4.4	
	0.0018/0.018	7.460	0.88764	$64^3 \times 144$	827	4.3	
0.045	0.0028/0.014	7.810	0.89511	$64^3 \times 192$	801	4.6	
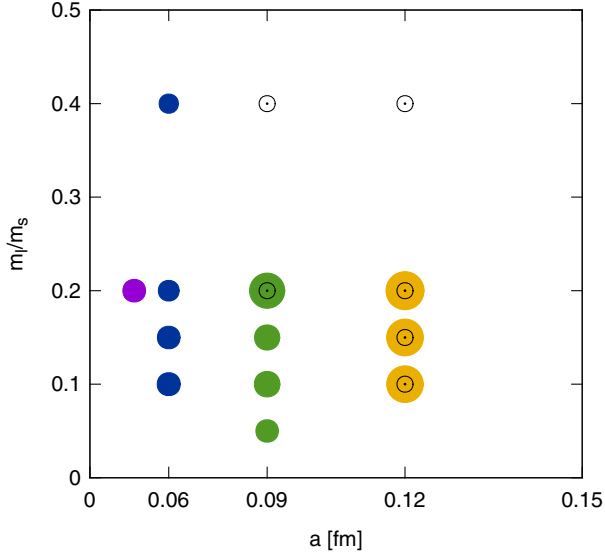
FIG. 1 (color online).   Lattice spacings and light-quark masses used in this analysis. The area of each filled disk is proportional to the number of configurations in the ensemble. Open black circles indicate ensembles use in the analysis of Ref. [5]; those with $(a, m'_l/m'_h) = (0.12 \text{ fm}, 0.4)$ and $(0.09 \text{ fm}, 0.4)$ used in Ref. [5] (open circles without disks) are not used in this analysis.

ensembles have four different lattice spacings ranging from $a \approx 0.12$ fm to $a \approx 0.045$ fm with several light sea-quark masses at most lattice spacings in the range $0.05 \leq am'_l/am'_h \leq 0.4$. The parameter range is shown in Fig. 1. We use the Symanzik-improved gauge action [22–24] for the gluons and the tadpole-improved (asqtad) staggered action [25–30] for the $2+1$ flavors of dynamical sea quarks and for the light valence quarks. Both Table I and Fig. 1 also indicate the ensembles used in the previous Fermilab/MILC calculation [5]. The current analysis benefits from an almost quadrupled increase in the statistics over that of Ref. [5], as well as finer lattice spacings and lighter sea-quark masses. All ensembles have large enough spatial volume, $M_\pi L \geq 3.8$, such that the systematic error due to finite-size effects is negligible compared to other uncertainties.

   In this calculation, we work in the full-QCD limit, so that the light valence-quark masses am_l are the same as the light sea-quark masses am'_l, which are degenerate. For the bottom quarks, we use the Fermilab interpretation [31] of the Sheikholeslami-Wohlert clover action [32]. In Table II, we list parameters for the valence quarks.

   Table III lists the values of r_1/a on each ensemble, along with other derived parameters, where r_1 is the characteristic distance between two static quarks such that the force between them satisfies $r_1^2 F(r_1) = 1.0$ [33,34]. The absolute lattice scale r_1 is obtained by comparing the Particle Data Group value of f_π with lattice calculations of $r_1 f_\pi$ from MILC [35] and HPQCD [36], yielding the absolute scale $r_1 = 0.3117(22)$ fm [37]. This value is consistent with the

TABLE II.   Heavy-quark masses and other parameters used in the simulation. Starting in the third column: The clover parameter c_{SW}, the simulation b-quark mass parameter κ'_b, the current rotation parameter d'_1, the number of sources N_{src}, and the two source-sink separations T. Note that we use the same valence light-quark mass as m'_l in the sea except for the $a = 0.09$ fm, $m'_l/m'_h = 0.00465/0.031$ ensemble, where a slightly different valence mass $am_l = 0.0047$ is used.

$\approx a$ (fm)	am'_l/am'_h	c_{SW}	κ'_b	d'_1	N_{src}	T
0.12	0.01/0.05	1.531	0.0901	0.09334	4	18,19
	0.007/0.05	1.530	0.0901	0.09332	4	18,19
	0.005/0.05	1.530	0.0901	0.09332	4	18,19
0.09	0.0062/0.031	1.476	0.0979	0.09677	4	25,26
	0.00465/0.031	1.477	0.0977	0.09671	4	25,26
	0.0031/0.031	1.478	0.0976	0.09669	4	25,26
	0.00155/0.031	1.4784	0.0976	0.09669	4	25,26
0.06	0.0072/0.018	1.4276	0.1048	0.09636	4	36,37
	0.0036/0.018	1.4287	0.1052	0.09631	4	36,37
	0.0025/0.018	1.4293	0.1052	0.09633	4	36,37
	0.0018/0.018	1.4298	0.1052	0.09635	4	36,37
0.045	0.0028/0.014	1.3943	0.1143	0.08864	4	48,49

independent, but less precise, determination $r_1 = 0.323(9)$ from RBC/UKQCD using domain-wall fermions [38].

C. Currents and correlation functions

   We calculate the two-point and three-point functions

$$C_P(t;\boldsymbol{p}) = \sum_{\boldsymbol{x}} e^{i\boldsymbol{p}\cdot\boldsymbol{x}} \langle O_P(0,\boldsymbol{0}) O_P^\dagger(t,\boldsymbol{x}) \rangle \quad \text{and} \quad (2.9)$$

$$C_J(t,T;\boldsymbol{p}) = \sum_{\boldsymbol{x},\boldsymbol{y}} e^{i\boldsymbol{p}\cdot\boldsymbol{y}} \langle O_\pi(0,\boldsymbol{0}) J(t,\boldsymbol{y}) O_B^\dagger(T,\boldsymbol{x}) \rangle, \quad (2.10)$$

TABLE III.   Derived parameters from the simulation. Starting in the third column: Relative scale r_1/a, the Goldstone pion mass M_π, root-mean-square (rms) pion mass M_π^{rms}, and the critical hopping parameter κ_{crit} which enters our definition of the heavy-quark mass.

$\approx a$ (fm)	am'_l/am'_h	r_1/a	M_π (MeV)	M_π^{rms} (MeV)	κ_{crit}
0.12	0.01/0.05	2.7386	389	532	0.14091
	0.007/0.05	2.7386	327	488	0.14095
	0.005/0.05	2.7386	277	456	0.14096
0.09	0.0062/0.031	3.7887	354	413	0.139119
	0.00465/0.031	3.7716	307	374	0.139134
	0.0031/0.031	3.7546	249	329	0.139173
	0.00155/0.031	3.7376	177	277	0.139190
0.06	0.0072/0.018	5.3991	450	466	0.137582
	0.0036/0.018	5.3531	316	340	0.137632
	0.0025/0.018	5.3302	264	291	0.137667
	0.0018/0.018	5.3073	224	255	0.137678
0.045	0.0028/0.014	7.2082	324	331	0.136640

where $P = B$, π labels the pseudoscalar meson, the operators $O_P(O_P^\dagger)$ annihilate (create) the states with the quantum numbers of the pseudoscalar meson P on the lattice, and $J = V^\mu$, $T^{\mu\nu}$ are the lattice currents.

For the B meson, we use a mixed-action interpolating operator O_B which is a combination of a Wilson clover bottom quark and a staggered light quark [5]:

$$O_B(x) = \sum_y \bar{\psi}(y) S(y,x) \gamma_5 \Omega(x) \chi(x), \quad (2.11)$$

where $\Omega(x) = \gamma_1^{x_1} \gamma_2^{x_2} \gamma_3^{x_3} \gamma_4^{x_4}$, $x = (\boldsymbol{x}, t)$, and $S(x,y)$ is a smearing function. For the pion, we use the operator

$$O_\pi(x) = (-1)^{\sum_{i=1}^4 x_i} \bar{\chi}(x) \chi(x), \quad (2.12)$$

which is constructed from two 1-component staggered quarks.

The current operators are constructed in a similar way:

$$V^\mu(x) = \bar{\Psi}(x) \gamma^\mu \Omega(x) \chi(x) \quad \text{and} \quad (2.13)$$

$$T^{\mu\nu}(x) = \bar{\Psi}(x) \sigma^{\mu\nu} \Omega(x) \chi(x), \quad (2.14)$$

where the heavy quark field spinor Ψ is rotated to remove tree-level $O(a)$ discretization effects, via [31]

$$\Psi(x) = (1 + a d_1 \boldsymbol{\gamma} \cdot \boldsymbol{D}_{\text{lat}}) \psi. \quad (2.15)$$

Figure 2 illustrates the three-point correlation function used to obtain the lattice form factors. The current operator J is inserted between the b- and l-quark lines. The three-point functions depend on both the current insertion time t and the temporal separation T between the π and B mesons. The signal-to-noise ratio is largely determined by T. A convenient approach is to fix the source-sink separation T in the simulations and then insert the current operators at every time slice in between. The source-sink separations T
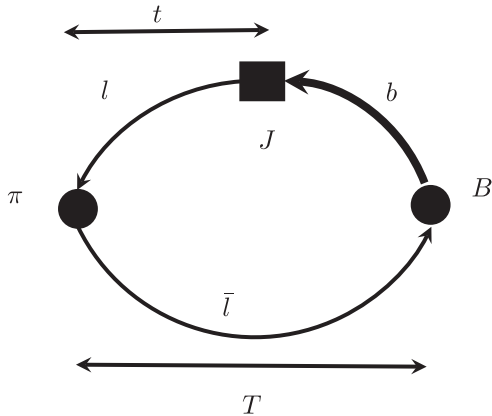

FIG. 2. Illustrative diagram for the three-point correlation functions.

at different lattice spacings, sea-quark masses, and recoil momenta are chosen to be approximately the same in physical units. To minimize statistical uncertainties and reduce excited-state contamination, we tested data with different source-sink separations before choosing those shown in Table II. The B meson is at rest in our simulation, while the daughter pion is either at rest or has a small three-momentum. The light-quark propagator is computed from a point source so that one inversion of the Dirac operator can be used to obtain multiple momenta. The spatial source location is varied randomly from one configuration to the next to minimize autocorrelations. The b-quark source is always implemented with smearing based on a Richardson 1S wave function [39] after fixing to Coulomb gauge. We compute both the two-point function $C_\pi(t; \boldsymbol{p})$ and the three-point function $C_J(t, T; \boldsymbol{p})$ at several of the lowest possible pion momenta in a finite box: $\boldsymbol{p} = (2\pi/L)(0,0,0)$, $(2\pi/L)(1,0,0)$, $(2\pi/L)(1,1,0)$, $(2\pi/L)(1,1,1)$, and $(2\pi/L)(2,0,0)$, where contributions from each momentum are averaged over permutations of components. We find the correlation functions with momentum $(2\pi/L)(2,0,0)$ too noisy to be useful, so we exclude these data from our analysis.

D. Two-point and three-point correlator fits

In this subsection, we describe how to extract the desired matrix element from two- and three-point correlation functions. With our choice for the valence-quark actions and for the interpolating operators, the two- and three-point functions take the form [40]

$$C_P(t; \boldsymbol{p}) = \sum_{n=0}^\infty (-1)^{n(t+1)} |Z_P^{(n)}(\boldsymbol{p})|^2$$
$$\times [e^{-E_P^{(n)}(\boldsymbol{p}) t} + e^{-E_P^{(n)}(\boldsymbol{p})(N_t - t)}], \quad (2.16)$$

$$C_J(t, T; \boldsymbol{p}) = \sum_{m,n=0}^\infty (-1)^{m(t+1)} (-1)^{n(T-t-1)} Z_\pi^{(m)}(\boldsymbol{p})$$
$$\times \mathcal{M}_J^{(mn)} Z_B^{(n)}(\boldsymbol{0}) e^{-E_\pi^{(m)}(\boldsymbol{p}) t - M_B^{(n)}(T-t)}, \quad (2.17)$$

where N_t is the temporal length of the lattice, and

$$Z_P^{(n)}(\boldsymbol{p}) = \frac{|\langle 0 | O_P | P^{(n)}(\boldsymbol{p}) \rangle|}{\sqrt{2 E_P^{(n)}(\boldsymbol{p})}}, \quad (2.18)$$

$$\mathcal{M}_J^{(mn)} = \frac{\langle \pi^{(m)}(\boldsymbol{p}) | J | B^{(n)} \rangle}{\sqrt{2 E_\pi^{(m)}(\boldsymbol{p})} \sqrt{2 M_B^{(n)}}}. \quad (2.19)$$

Note that due to the staggered action used for the light quarks, the meson interpolating operators also couple to the positive-parity (scalar) states which oscillate in Euclidean times t and T with the factors $(-1)^{n(t+1)}$ and $(-1)^{n(T-t)}$.
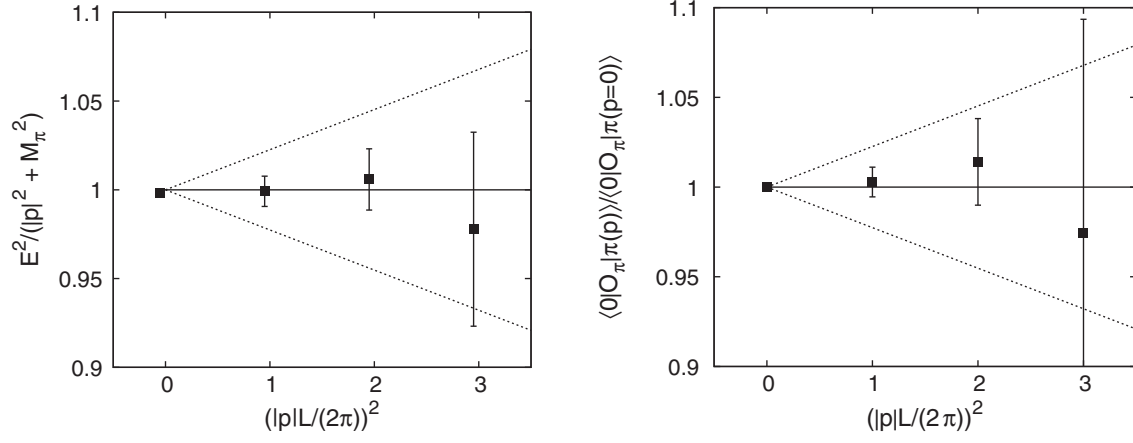
FIG. 3.   Dispersion-relation tests on the ensemble $a \approx 0.12$ fm, $m'_l/m'_h = 0.1$. Left: Fit results of $E_\pi^2(\boldsymbol{p})$ from two-point functions are compared with the continuum dispersion relation $|\boldsymbol{p}|^2 + M_\pi^2$. Right: Wave-function overlaps $\langle 0|O_\pi|\pi(\boldsymbol{p})\rangle$ at different momenta are compared. The dotted lines show the expected size of the leading momentum-dependent discretization errors based on power counting, which are of $\mathcal{O}(\alpha_s^2|\boldsymbol{p}|^2 a^2)$.

Our goal is to extract $\mathcal{M}_J^{(00)}$, the ground-state matrix element from these correlation functions. To suppress the contributions from the positive-parity states to the ratio, we follow the averaging procedure of Ref. [5], which exploits the oscillating sign in their Euclidean time dependence. The time averages can be thought of as a smearing over neighboring time slices $\{t, t+1, t+2\} \times \{T, T+1\}$ to significantly reduce the overlap with opposite-parity states. Denoting the averaged correlators by $\overline{C_P}$ and $\overline{C_J}$, we then use the ratio [5]

$$R_J(t, T; \boldsymbol{p}) = \frac{\overline{C_J}(t, T; \boldsymbol{p})}{\sqrt{\overline{C_\pi}(t; \boldsymbol{p})\, \overline{C_B}(T-t; \boldsymbol{0})}} \sqrt{\frac{2E_\pi^{(0)}(\boldsymbol{p})}{e^{-E_\pi^{(0)}(\boldsymbol{p})t - M_B^{(0)}(T-t)}}},$$

(2.20)

where $E_\pi^{(0)}(\boldsymbol{p})$ and $M_B^{(0)}$ are the ground-state pion energy and B-meson rest mass, respectively. The uncertainty in the B-meson rest mass has significant impact on the ratio R_J, so we follow a two-step procedure. We first determine the pion and B-meson ground-state energy as precisely as possible using the corresponding two-point functions. We then feed these ground-state energies into the ratio R_J, preserving the correlations with jackknife resampling.

For the pion two-point functions at zero momentum, the oscillating states—the terms in Eq. (2.16) with odd powers of (-1)—do not appear. Thus, we fit the pion two-point functions using Eq. (2.16) with the lowest two nonoscillating states $(n = 0, 2)$. For the two-point functions with nonzero momentum, the contribution from oscillating states is small but noticeable. We find that we only need to include the lowest three states $(n = 0, 1, 2)$ in the fits. Because the momenta we consider are typically small compared to $2\pi/a$, the continuum dispersion relation is satisfied within statistical errors, as shown in Fig. 3. In the

main analysis, we therefore use the mass M_π from the zero-momentum fit and the continuum dispersion relation to set $E_\pi^{(0)}(\boldsymbol{p}) = \sqrt{|\boldsymbol{p}|^2 + M_\pi^2}$ for nonzero momentum. Because the zero-momentum energy has significantly smaller statistical error than that of nonzero momentum, using this choice and the dispersion relation for nonzero-momentum energy leads to a more stable and precise determination of $\mathcal{M}_J^{(00)}$. Table IV lists the relevant fit ranges for the two-point fits. In the two-point correlators (except the zero-momentum-pion two-point correlators), the noise grows rapidly with increasing t, the distance away from the pion source in the temporal direction. The data points at large t are not useful, and including them would lead to a larger covariance matrix which would be difficult to resolve given the limited number of configurations. We choose the upper end of the fit ranges t_{max} such that the relative error does not exceed 20%. The lower end t_{min} is chosen such that the excited state contamination is sufficiently small, i.e., the

TABLE IV.   Fit ranges $[t_{min}, t_{max}]$ of the two-point correlator fits used to obtain the rest masses of the pion and B mesons.

| $\approx a$ (fm)	am'_l/am'_h	$C_\pi(2+0)$	$C_B^{(1S)}(1+1)$
0.12	0.01/0.05	[6, 30]	[9, 21]
	0.007/0.05	[6, 30]	[9, 21]
	0.005/0.05	[6, 30]	[9, 21]
0.09	0.0062/0.031	[9, 47]	[12, 32]
	0.00465/0.031	[9, 47]	[12, 29]
	0.0031/0.031	[9, 47]	[13, 29]
	0.00155/0.031	[9, 47]	[14, 29]
0.06	0.0072/0.018	[13, 71]	[14, 41]
	0.0036/0.018	[13, 71]	[14, 41]
	0.0025/0.018	[13, 71]	[14, 41]
	0.0018/0.018	[13, 71]	[15, 41]
0.045	0.0028/0.014	[17, 74]	[17, 61]
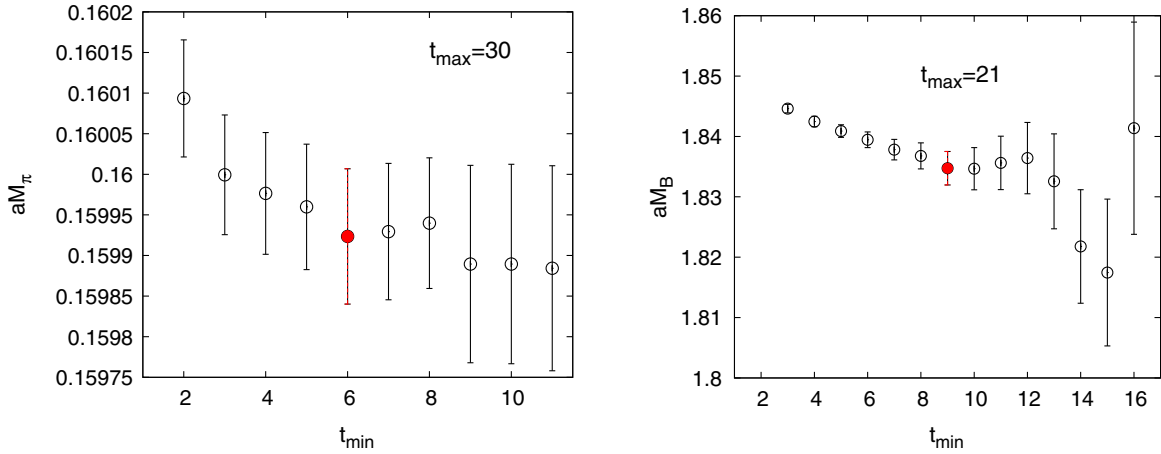
FIG. 4 (color online).   Pion (left) and B-meson (right) mass in lattice units from the two-point correlator fits versus different choices of $t_{\min}$ for the $a \approx 0.12$ fm, $m'_l/m'_h = 0.1$ ensemble. The $t_{\min}$ marked in red (filled) is that of our preferred fit. The pion and B-meson correlators are fit to $2 + 0$ and $1 + 1$ states with $t_{\max} = 30, 21$, respectively.

resulting central values of the ground-state energy are stable against variations in $t_{\min}$, as shown in Fig. 4 (left).

In our analysis, there are two places where quantities from the B-meson two-point functions are needed. The first is for $M_B^{(0)}$ in Eq. (2.20). The second is for the B-meson

excited-state energy in Eq. (2.21) below. For the determination of $M_B^{(0)}$ in Eq. (2.20), we use two-point functions constructed with a 1S-smearing function in the interpolating operators for the source and sink. The 1S-smeared operator has good overlap with the ground state and a much
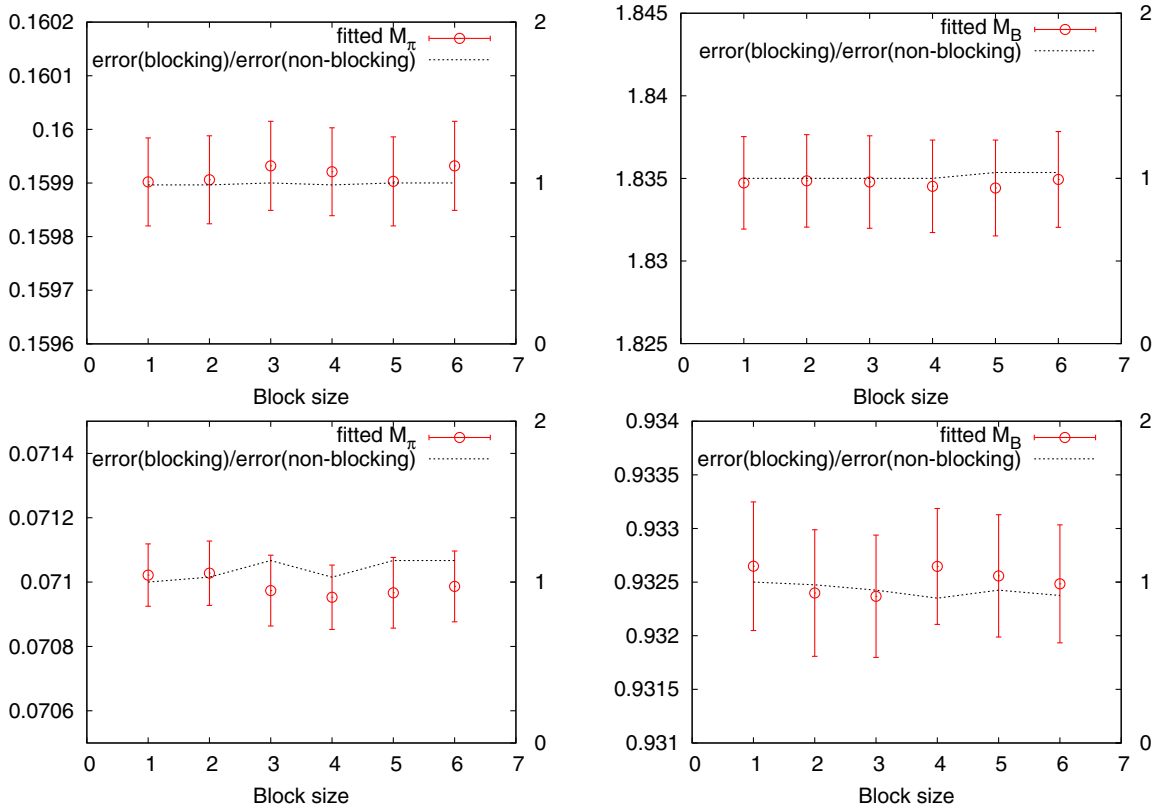
FIG. 5 (color online).   Fitted M_π and M_B in lattice units versus the block size for the $a \approx 0.12$ fm, $m'_l/m'_h = 0.1$ ensemble (top) and for the $a \approx 0.045$ fm, $m'_l/m'_h = 0.2$ ensemble (bottom). The dashed line shows the ratio of the fit errors from the blocking and nonblocking data, which can be read off from the right y axis.

smaller overlap with the excited states than the local source operator, thus reducing excited-state contributions to the corresponding correlators. We fit the 1S-1S-smeared B-meson two-point correlators with relatively large $t_{\min}$ to only two states [$n < 2$ in Eq. (2.16)]. To choose $t_{\max}$, we again apply the 20% rule on the relative error. The lower bound $t_{\min}$ is chosen in a manner similar to the pion two-point fits, and the stability plot is shown in Fig. 4 (right). The chosen fit ranges are shown in Table IV.

We test for autocorrelations by blocking the configurations on each ensemble with different block sizes, and then using a single-elimination jackknife procedure to propagate the statistical error to the two-point correlator fits for M_π and $M_B^{(0)}$. We do not observe any noticeable autocorrelations in all the ensembles we use, as illustrated in Fig. 5 for the coarsest and finest ensembles, and choose not to block the data.

The ratios in Eq. (2.20) have the advantage that the wave-function overlap factors Z_P cancel, but the tradeoff is that we need an additional factor—the square-root term on the right-hand side—to remove the leading t dependence in the ratio. If the lowest-lying states dominated the ratio R_J, then it would be constant in t and proportional to the lattice form factor f_J. The subscript J now runs over $\perp$, $\|$, and T, corresponding to the operators V^i, V^4, and T^{4i}, respectively. Our previous analysis employed a simple plateau fit constant in time. With our improved statistics, the small excited-state contributions to the ratio are significant and cannot be neglected. On the other hand, even with our improved statistics, we find that contributions to R_J from wrong-parity states are still negligible. We use two different fit strategies to remove excited-state contributions and use the consistency between them as an added check that any remaining excited-state contamination is negligibly small.

The first strategy starts with the ratio in Eq. (2.20) and minimally extends the plateau fitting scheme by including the first excited state of the B meson in the following form:

$$\frac{R_J(t)}{h_J} = f_J^{\text{lat}}[1 + \mathcal{A}_J e^{-\Delta M_B(T-t)}], \qquad (2.21)$$

where $\mathcal{A}_J$ and f_J^{lat} are unconstrained fit parameters, $\Delta M_B \equiv M_B^{(2)} - M_B^{(0)}$ is the lowest-energy splitting of the pseudoscalar B meson, and the prefactors are $h_\| = 1$, $h_\perp = p_\pi^i$ and $h_T = (\sqrt{2M_B}p_\pi^i)/(M_B + M_\pi)$. We choose the fit ranges for R_J such that contributions from pion excited states to R_J can be neglected. The fit parameter ΔM_B is determined by the B-meson two-point correlators. In practice, we fit the ratio in Eq. (2.21) along with the B-meson two-point correlation functions with ΔM_B as a common parameter. We find it beneficial in the combined fit to include both the local and smeared two-point correlation functions. We use $2 + 2$ states for both correlators, but use a different set of fit ranges (listed in Table V). The results of these two-point fits

TABLE V. The fit ranges $[t_{\min}, t_{\max}]$ of the combined two-point and three-point ratio fits to obtain the lattice form factors.

$\approx a$ (fm)	am'_l/am'_h	$C_B^{(d)}$	$C_B^{(1S)}$	$R_\|$	$R_\perp$	R_T
0.12	0.01/0.05	[9, 23]	[7, 21]	[6, 12]	[6, 12]	[6, 12]
	0.007/0.05	[9, 23]	[7, 21]	[6, 12]	[6, 12]	[6, 12]
	0.005/0.05	[9, 23]	[7, 21]	[6, 12]	[6, 12]	[6, 12]
0.09	0.0062/0.031	[12, 32]	[9, 32]	[9, 16]	[9, 16]	[9, 16]
	0.00465/0.031	[12, 32]	[9, 29]	[9, 16]	[9, 16]	[9, 16]
	0.0031/0.031	[12, 32]	[9, 29]	[9, 16]	[9, 16]	[9, 16]
	0.00155/0.031	[12, 29]	[9, 29]	[9, 15]	[9, 15]	[9, 15]
0.06	0.0072/0.018	[13, 41]	[9, 41]	[12, 22]	[12, 22]	[12, 22]
	0.0036/0.018	[13, 41]	[9, 41]	[12, 22]	[12, 22]	[12, 22]
	0.0025/0.018	[13, 41]	[9, 41]	[12, 22]	[12, 22]	[12, 22]
	0.0018/0.018	[13, 41]	[9, 41]	[12, 21]	[12, 21]	[12, 21]
0.045	0.0028/0.014	[16, 61]	[10, 61]	[16, 26]	[16, 26]	[16, 26]

are shown in Fig. 6. The agreement in the B-meson energies between the separate and combined fits is very good, but the combined fit leads to smaller errors.

To summarize our strategy, for the case of zero momentum, we fit the ratio $R_\|(t)$ together with the local and smeared B-meson two-point correlators $C_B^{(d)}$, $C_B^{(1S)}$ simultaneously. For nonzero momentum $\boldsymbol{p}$, ΔM_B is common to all three ratios, $R_\|, R_\perp, R_T$. Thus, we perform a combined fit to the five quantities $R_\|, R_\perp, R_T, C_B^{(d)}$ and $C_B^{(1S)}$. Figure 7 shows an example of these fits. Figure 8 shows the stability plots of $R_\perp$ against the variations in the fit ranges of the ratio fits, and the variations in the fit ranges of both two-point correlators. The preferred fit ranges are set to be in the stable region upon these variations.

Our second fit strategy includes excited-state contributions from both the pion and the B meson. It starts with a different ratio, without time averages, which ensures that there are enough data points to constrain all the parameters:
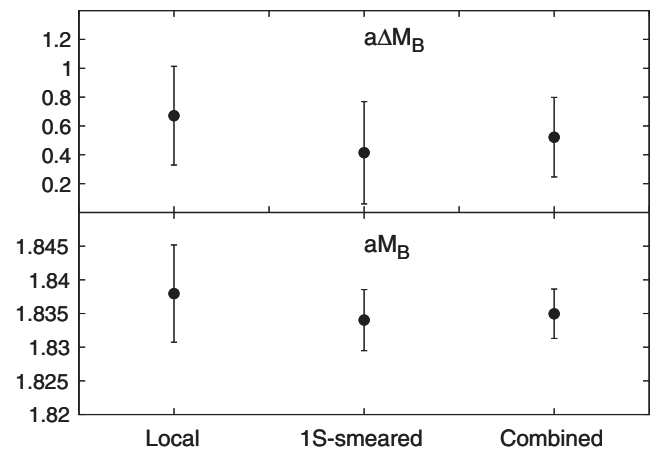

FIG. 6. Ground-state energy (bottom) and the first excited-state splitting (top) of the B meson on the $a \approx 0.12$ fm, $m'_l/m'_h = 0.1$ ensemble, from different fits to local, 1S-smeared, and both two-point correlators.
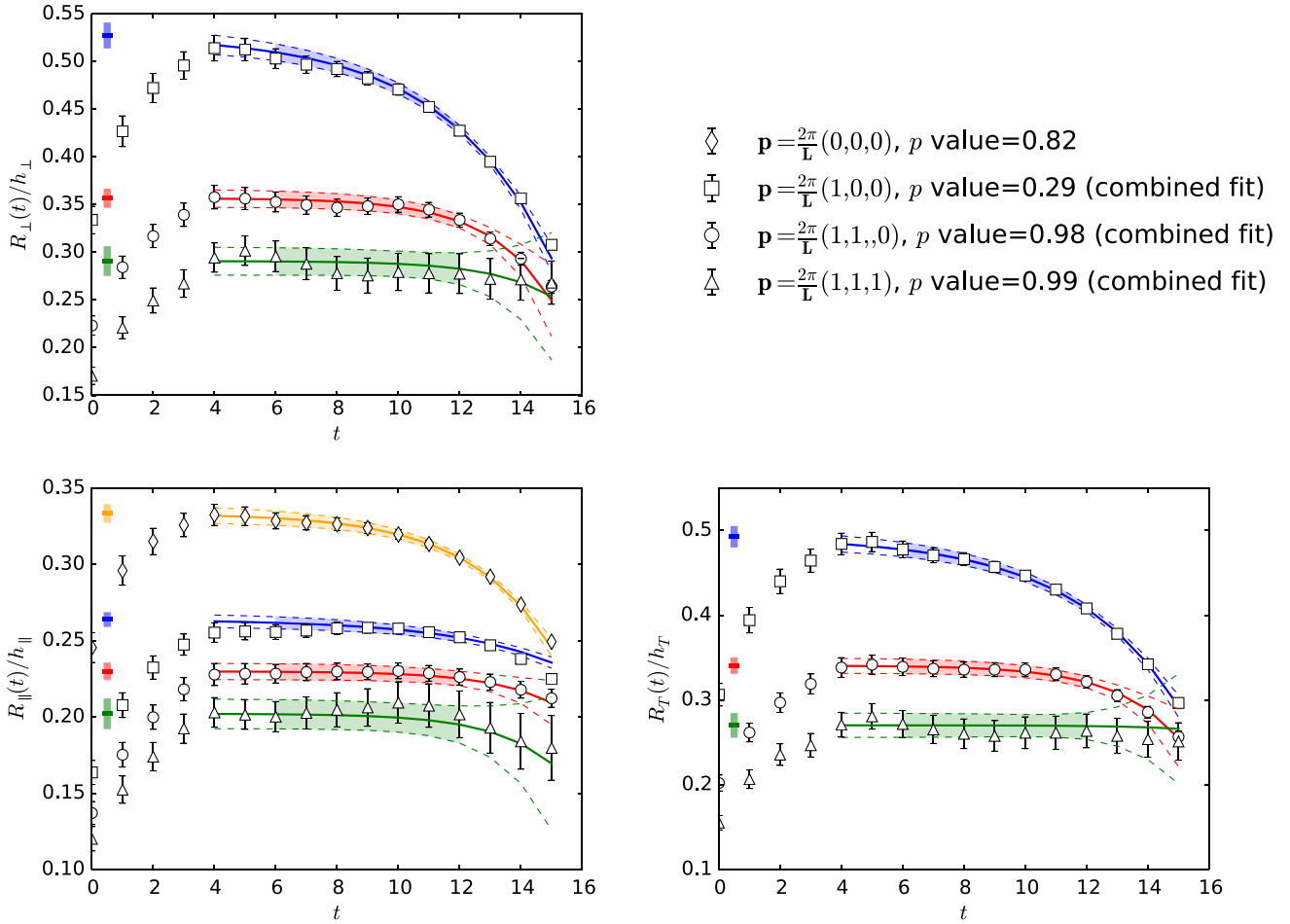
FIG. 7 (color online).   Fits of ratios $R_\perp/h_\perp$ (top left), $R_\parallel/h_\parallel$ (bottom left) and R_T/h_T (bottom right) for the $a \approx 0.12$ fm, $m'_l/m'_h = 0.1$ ensemble. The open data points with error bars are the ratios constructed from two- and three-point correlators with various momenta. The fit results are shown as solid lines with dashed error widths. The shaded bands indicate the range of data employed in the fit. The resulting lattice form factors f_J are shown by the colored bars on the left of the plots.
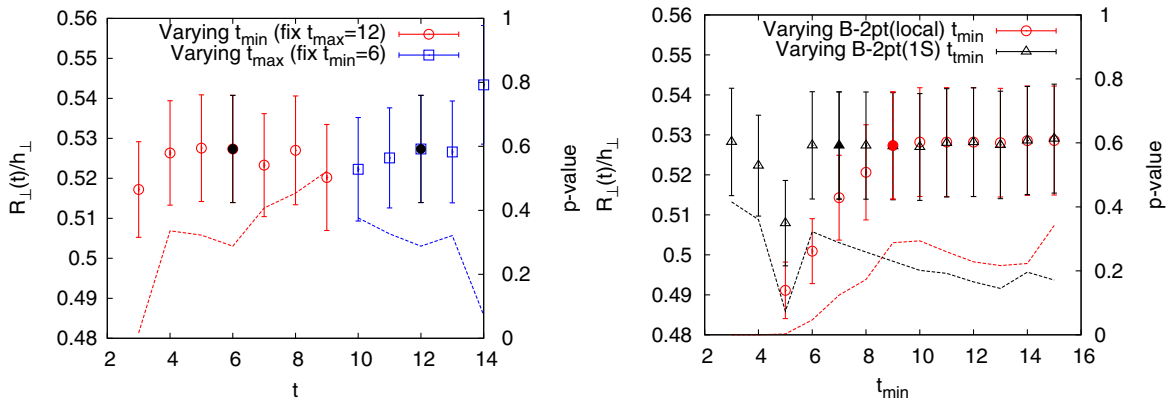
FIG. 8 (color online).   Left: Fitted ratio $R_\perp/h_\perp$ on the $a \approx 0.12$ fm, $m'_l/m'_h = 0.1$ ensemble with momentum $\boldsymbol{p} = (2\pi/L)(1,0,0)$ for different combinations of $t_{\min}, t_{\max}$ of the three-point correlator in the combined fit, where circles are results of varying $t_{\min}$ with fixed $t_{\max} = 12$ and squares are those of varying $t_{\max}$ with fixed $t_{\min} = 6$. Right: The same $R_\perp/h_\perp$ upon variations of $t_{\min}$ of the two B-meson two-point correlators (local and $1S$-smeared) in the combined fit, where $t_{\max}$ is given in Table V. The filled points in both plots show the preferred fit ranges, and the dashed lines indicate the p values of the fits.
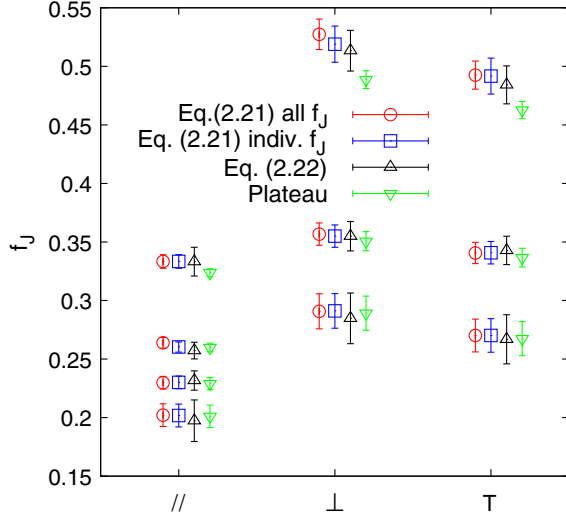
FIG. 9 (color online).   Fitted lattice form factors f_J at different momenta: From top to bottom, $(2\pi/L)(0,0,0)$ ($f_\parallel$ only), $(2\pi/L)(1,0,0)$, $(2\pi/L)(1,1,0)$ and $(2\pi/L)(1,1,1)$. Each compares the following different fit schemes: Separate (squares) or combined (circles) fits of the three lattice form factors f_J using Eq. (2.21), a fit including the full first excited states as defined in Eq. (2.22) (upward-pointing triangles) and the simple plateau fit (downward-pointing triangles).

$$\tilde{R}_J(t) = \frac{C_J(t,T;\boldsymbol{p})}{C_\pi(t;\boldsymbol{p})C_B(T-t;\boldsymbol{0})}, \qquad (2.22)$$

where the two- and three-point correlators are defined in Eqs. (2.9) and (2.10). We fit $\tilde{R}_J(t)$ with all the possible states with $m, n \leq 2$ in Eqs. (2.16) and (2.17), combining the fits to the pion and B-meson two-point correlators. We compare the fit results of the two different fit schemes in Fig. 9. The first (simple) fit model described in Eq. (2.21) gives, fitting either simultaneously or individually to the three lattice form factors f_J, results that are consistent with the second fit model that includes the full set of first excited states in Eq. (2.22). In contrast, the plateau fits to R_J defined in Eq. (2.20) yield results that are as much as one statistical σ smaller. In summary, we find that the first fit strategy described by Eq. (2.21) is sufficient to remove contributions from excited states, and we therefore adopt this method for the main analysis.

E. Matching

We match the lattice currents to continuum QCD with the relation

$$\mathcal{J} \doteq Z_{J_{bl}}J, \qquad (2.23)$$

where $\mathcal{J}$ and J denote the vector or tensor currents in the continuum and lattice theories, respectively, and "$\doteq$" means "has the same matrix elements" [41]. We calculate

the current renormalization with the mostly nonperturbative renormalization method [18,42],

$$Z_{J_{bl}} = \rho_{J_{bl}}\sqrt{Z_{V^4_{bb}}Z_{V^4_{ll}}}, \qquad (2.24)$$

where $Z_{V^4_{bb}}$ and $Z_{V^4_{ll}}$ are the matching factors for the corresponding flavor-conserving vector currents. These factors capture most of the current renormalization. The remaining flavor off-diagonal contribution to the matching factor, $\rho_{J_{bl}}$, is close to unity.

We calculate the factors $Z_{V^4_{bb}}$ and $Z_{V^4_{ll}}$ nonperturbatively for each ensemble by computing the matrix elements of the flavor-conserving vector currents and using the relations

$$1 = Z_{V^4_{ll}}\langle\pi|V^4_{ll}|\pi\rangle, \qquad (2.25)$$

$$1 = Z_{V^4_{bb}}\langle B_s|V^4_{bb}|B_s\rangle, \qquad (2.26)$$

where the lattice current V^4_{ll} is a bilinear of light staggered quark fields and V^4_{bb} is a bilinear of clover heavy-quark fields. The factors $Z_{V^4_{bb}}$ and $Z_{V^4_{ll}}$ are listed in Table VI. Because there is very little m_l dependence in the factor $Z_{V^4_{ll}}$, we use the same $Z_{V^4_{ll}}$ for ensembles with different light quark masses but the same lattice spacing. The factor $Z_{V^4_{bb}}$ depends crucially on the heavy b-quark mass, though it has negligible light-quark mass dependence.

We use lattice perturbation theory [43] to compute the remaining renormalization factors ρ_J at one loop. Due to the cancellation of the tadpole contributions in the radiative corrections to the left and right sides of Eq. (2.24), the factors ρ_J are very close to 1. They have the perturbative expansion

$$\rho_J = 1 + \alpha_V(q^*)\rho_J^{[1]} + O(\alpha_V^2), \qquad (2.27)$$

where we take the strong coupling in the V scheme [43] at a scale q^* that corresponds to the typical gluon loop momentum. In practice, we choose $q^* = 2/a$. The details of the calculation of the one-loop coefficients $\rho_J^{[1]}$ will be presented elsewhere. The values used in this work are shown in Table VI.

F. Heavy-quark mass correction

In the clover action, the hopping parameter κ_b corresponds to the bare b-quark mass. When we started generating data for this analysis, we had a good estimate for the bottom-quark κ'_b on each ensemble, but not the final tuned values, which were obtained as described in Appendix C of Ref. [44]. We therefore need to adjust the form factors *a posteriori* to account for the slightly mistuned values of κ_b.

TABLE VI.   The parameters for the renormalization of the form factors. The first two columns label the ensemble with its approximate lattice spacing and the sea light- and strange-quark mass ratio. The third column is the simulation κ_b'. The fourth and fifth columns are the nonperturbative heavy-heavy and light-light renormalization factors $Z_{V^4_{bb}}$, $Z_{V^4_{ll}}$. The sixth, seventh, and eighth columns are the one-loop estimates of ρ_{V^4}, ρ_{V^i}, and ρ_T, respectively. The tensor current has a nonzero anomalous dimension; the numbers reported here match to the $\overline{\text{MS}}$ scheme at renormalization scale $\mu = m_2$, which corresponds to the pole mass. Note that with our convention $Z_{V^4_{ll}}$ and $Z_{V^4_{bb}}$ are normalized so that at tree level $Z^{[0]}_{V^4_{ll}} = 2$ and $Z^{[0]}_{V^4_{bb}} = 1 - 6u_0\kappa_b'$ [37]. As a result, $Z_{V^{bb}_4}$ only approaches 1 in the limit $m_b \to \infty$.

$\approx a$ (fm)	am_l'/am_h'	κ_b'	$Z_{V^4_{bb}}$	$Z_{V^4_{ll}}$	$\rho_{V^4_{bl}}$	$\rho_{V^i_{bl}}$	$\rho_{T_{bl}}$
0.12	0.01/0.05	0.0901	0.5015(8)	1.741(3)	1.006214	0.973023	1.033350
	0.007/0.05	0.0901	0.5015(8)	1.741(3)	1.006252	0.973109	1.033280
	0.005/0.05	0.0901	0.5015(8)	1.741(3)	1.006197	0.973082	1.033270
	0.01/0.05	0.0860	0.5246(9)	1.741(3)	1.012999	0.977290	1.030650
	0.01/0.05	0.0820	0.5469(10)	1.741(3)	1.018261	0.980129	1.028960
0.09	0.0062/0.031	0.0979	0.4519(15)	1.776(5)	0.999308	0.975822	1.036590
	0.00465/0.031	0.0977	0.4530(15)	1.776(5)	0.999405	0.975775	1.036390
	0.0031/0.031	0.0976	0.4536(15)	1.776(5)	0.999441	0.975744	1.036350
	0.00155/0.031	0.0976	0.4536(15)	1.776(5)	0.999416	0.975703	1.036390
0.06	0.0072/0.018	0.1048	0.4089(21)	1.807(7)	0.995605	0.979279	1.042390
	0.0036/0.018	0.1052	0.4065(21)	1.807(7)	0.995371	0.979260	1.043160
	0.0025/0.018	0.1052	0.4065(21)	1.807(7)	0.995350	0.979217	1.043190
	0.0018/0.018	0.1052	0.4065(21)	1.807(7)	0.995327	0.979176	1.043250
0.045	0.0028/0.014	0.1143	0.3564(65)	1.841(6)	0.994195	0.984351	1.058790

The κ_b parameters are adjusted so that the corresponding B_s kinetic masses match the experimentally measured value [44]. Table VII shows both the simulation and final tuned κ_b values. For some ensembles, the difference between the two is as large as 7σ of the statistical uncertainty associated with the tuning procedure. We study the κ_b dependence of the lattice form factors by generating data on the $a \approx 0.12$ fm, $m_l'/m_h' = 0.2$ ensemble, with two additional κ_b' values, 0.0860 and 0.0820, and all other simulation parameters unchanged. To generalize the κ_b dependence from this ensemble to others, we work with the quark kinetic mass m_2 instead of κ_b itself. We expand the form factor $f(f = f_{\perp,\parallel,T})$ in m_2^{-1} about a reference point $\bar{m}_2^{-1}$ (which corresponds to the tuned κ_b) as follows:

$$
\begin{aligned}
f(m_2^{-1}, a^2, m_l, E_\pi) &\approx f(\bar{m}_2^{-1}, a^2, m_l, E_\pi) \\
&\quad + \frac{\partial f(\bar{m}_2^{-1}, a^2, m_l, E_\pi)}{\partial \bar{m}_2^{-1}}(m_2^{-1} - \bar{m}_2^{-1}) \\
&= f(\bar{m}_2^{-1}, a^2, m_l, E_\pi) \\
&\quad \times \left[1 + \frac{1}{f}\frac{\partial f}{\partial \bar{m}_2^{-1}}(m_2^{-1} - \bar{m}_2^{-1})\right] \\
&= f(\bar{m}_2^{-1}, a^2, m_l, E_\pi) \\
&\quad \times \left[1 - \frac{\partial \ln f}{\partial \ln \bar{m}_2}\left(\frac{\bar{m}_2}{m_2} - 1\right)\right],
\end{aligned}
\tag{2.28}
$$

TABLE VII.   Parameters needed to apply heavy-quark mass corrections. The third column contains the value κ_b' used for the calculation; the fourth column contains the tuned value κ_b with its statistical error. Subsequent columns contain the percentage shift in m_2 and each of the form factors.

| $a(\approx$fm)	am_l'/am_h'	κ_b'	κ_b	$\frac{\Delta m_2}{m_2}$ (%)	$\frac{\Delta f_\perp}{f_\perp}$ (%)	$\frac{\Delta f_\parallel}{f_\parallel}$ (%)	$\frac{\Delta f_T}{f_T}$ (%)
0.12	0.01/0.05	0.0901	0.0868(9)	10.9	1.79	1.55	1.60
	0.007/0.05	0.0901	0.0868(9)	10.9	1.80	1.57	1.58
	0.005/0.05	0.0901	0.0868(9)	10.9	1.81	1.58	1.56
0.09	0.0062/0.031	0.0979	0.0967(8)	4.3	0.69	0.60	0.62
	0.00465/0.031	0.0977	0.0966(8)	3.9	0.63	0.55	0.56
	0.0031/0.031	0.0976	0.0965(8)	3.9	0.64	0.56	0.55
	0.00155/0.031	0.0976	0.0964(8)	4.2	0.70	0.61	0.59
0.06	0.0072/0.018	0.1048	0.1054(5)	−2.4	−0.37	−0.36	−0.44
	0.0036/0.018	0.1052	0.1052(5)	0.0	0.0	0.0	0.0
	0.0025/0.018	0.1052	0.1051(5)	0.4	0.06	0.06	0.06
	0.0018/0.018	0.1052	0.1050(5)	0.8	0.13	0.11	0.11
0.045	0.0028/0.014	0.1143	0.1116(4)	14.3	2.34	2.03	2.10
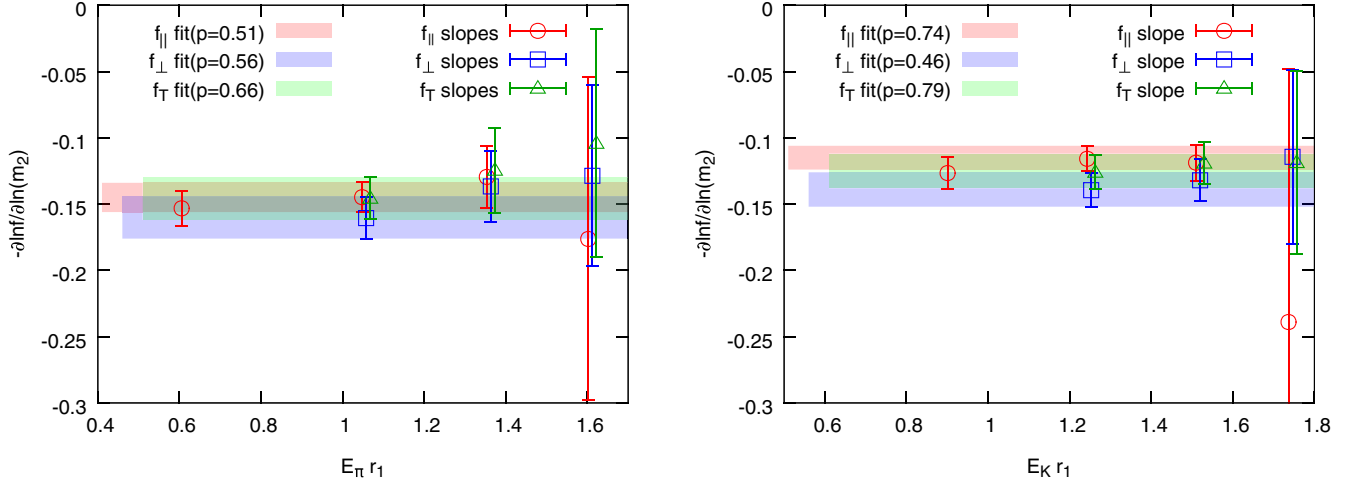
FIG. 10 (color online). The normalized slopes $-(\partial \ln f/\partial \ln \bar{m}_2)$ of the three different form factors $f_{\parallel,\perp,T}$ at several momenta for $B \to \pi$ (left) and $B \to K$ (right) semileptonic decays. The horizontal shaded error bands in each plot are the results of correlated fits to all momenta for each form factor.

where the masses and E_π are all in r_1 units. To obtain f at the reference point, we need to find the dimensionless normalized slope $-(\partial \ln f/\partial \ln \bar{m}_2)$.

We use exactly the same procedure as described in Sec. II D for $\kappa_b' = 0.0901$ to obtain the $B \to \pi\ell\nu$ form factors $f_{\parallel,\perp,T}$ for the additional values $\kappa_b' = 0.0860$ and 0.0820. We apply the matching factors given in Table VI. Finally, we take $\bar{m}_2$ to be the kinetic mass corresponding to $\kappa_b = 0.0868$ (the tuned kappa given in Table VII) and use it as the reference point. We fit each form factor at each momentum for the three data points to the linear form given in Eq. (2.28), taking $f(\bar{m}_2^{-1})$ and $-(\partial \ln f/\partial \ln \bar{m}_2)$ as fit parameters. The result is shown in Fig. 10 (left). As shown in the plot, the normalized slope $-(\partial \ln f/\partial \ln m_2)$ has a very mild E_π dependence. Therefore, for each form factor we perform a correlated fit to all momenta to obtain a single common normalized slope. The result is shown in Table VIII. Fitting the data to a linear form in E_π results in a slope statistically consistent with zero.

To examine the light-quark mass dependence of the normalized slopes, we repeat the same procedure for the $B \to K$ semileptonic form factors with a heavier daughter valence quark $am_s = 0.0349$, which is close to the physical strange-quark mass. The results are plotted in Fig. 10 (right). We fit the points of each form factor to a constant

and tabulate the results in Table VIII. Comparing the normalized slopes for $f^{B\to\pi}$ and $f^{B\to K}$, taking into account statistical correlations, we observe a mild but statistically significant light daughter-quark mass dependence. So we fit the slopes for $f^{B\to\pi}$ and $f^{B\to K}$ simultaneously to a linear form,

$$-\frac{\partial \ln f}{\partial \ln \bar{m}_2} = c + d\frac{m_l}{m_s}, \qquad (2.29)$$

where $m_l/m_s = 0.2$ and 1.0 for $f^{B\to\pi}$ and $f^{B\to K}$, respectively. The results for the parameters c and d are given in Table VIII. Note that the results in Table VIII are also used in Ref. [45].

We use the parameters c and d in Table VIII to determine the normalized slope $-(\partial \ln f/\partial \ln \bar{m}_2)$ for each ensemble. Although the dependence of the normalized slopes on the light daughter-quark mass is resolvable, the effects are small for the ensembles we use in the analysis (with light daughter-quark masses ranging from $0.05m_s$ to $0.4m_s$). We expect similarly small effects from the spectator-quark masses. We also expect that the lattice-spacing dependence of the normalized slopes is small, because it is a dimensionless ratio. We therefore correct each lattice form factor in each ensemble by a factor

TABLE VIII. Fitted normalized slopes to all momenta for $f^{B\to\pi}$, $f^{B\to K}$, and their combined fit with daughter-quark mass dependence.

| | $B \to \pi$ | | $B \to K$ | | Combined fit with m_l/m_s dependence | | |
	p value	$\frac{\partial \ln f}{\partial \ln \bar{m}_2}$	p value	$\frac{\partial \ln f}{\partial \ln \bar{m}_2}$	p value	c	d
$f_\perp$	0.56	0.145(11)	0.46	0.115(9)	0.4	$-0.146(11)$	0.032(3)
$f_\parallel$	0.51	0.160(16)	0.74	0.139(13)	0.84	$-0.165(17)$	0.025(8)
f_T	0.66	0.146(16)	0.79	0.126(13)	0.88	$-0.137(17)$	0.034(8)

$$1 + \frac{\Delta f}{f} = \left[1 - \frac{\partial \ln f}{\partial \ln \bar{m}_2}\left(\frac{\bar{m}_2}{m_2} - 1\right)\right]^{-1}, \quad (2.30)$$

where m_2 and $\bar{m}_2$ are the kinetic masses corresponding to the simulation κ_b' and tuned κ_b, respectively. The resulting relative shift for each ensemble is shown in Table VII. Although the corrections to κ_b itself are significant for some ensembles, the corresponding corrections to the form factors are much smaller ($\lesssim 2.3\%$), as a consequence of the small normalized slopes.

III. CHIRAL-CONTINUUM EXTRAPOLATION

Here we extrapolate the form factors at four lattice spacings with several unphysical light-quark masses to the continuum limit and physical light-quark mass. We use heavy-meson rooted staggered chiral perturbation theory (HMrSχPT) [46,47], in the hard-pion and SU(2) limits. We also incorporate heavy-quark discretization effects into the chiral-continuum extrapolation.

A. SU(2) staggered chiral perturbation theory in the hard-pion limit

The full-QCD next-to-leading-order (NLO) HMrSχPT expression for the semileptonic form factors can be written [46]

$$f_J^{\text{NLO}} = f_J^{(0)}[c_0^J(1 + \delta f_{J,\text{logs}}) + c_1^J \chi_{\text{val}} + c_2^J \chi_{\text{sea}} \\ + c_3^J \chi_E + c_4^J \chi_E^2 + c_5^J \chi_{a^2}], \quad (3.1)$$

where $J = \perp, \|, T$. Note that the expressions are in units of the mass-independent scale r_1, and the coefficients c_i^J have the dimension of $r_1^{-3/2}$. The leading-order terms are

$$f_{\perp,T}^{(0)} = \frac{1}{f_\pi}\frac{g_{B^*B\pi}}{E_\pi + \Delta_{B^*} + \delta D_{\text{logs}}}, \quad (3.2)$$

$$f_{\|}^{(0)} = \frac{1}{f_\pi}, \quad (3.3)$$

with $g_{B^*B\pi}$ the B^*-B-π coupling constant and $\Delta_{B^*} \equiv M_{B^*} - M_B$ the B^*-B mass splitting. The terms $\delta f_{J,\text{logs}}$ and δD_{logs} are the one-loop nonanalytic contributions in the chiral expansion, and depend upon the light pseudoscalar meson mass and energy [46]. Note that in the heavy-quark expansion f_T is proportional to $f_\perp$ up to $\mathcal{O}(1/m_b)$. We therefore use the same pole location and nonanalytic corrections for f_T as $f_\perp$. The terms analytic in χ_i are introduced to cancel the scale dependence arising from the nonanalytic contribution in Eq. (3.1). The dimensionless variables χ_i are proportional to the quark mass, pion energy, and lattice spacing. We define

$$\chi_{\text{val}} = \frac{2\mu m_l}{8\pi^2 f_\pi^2}, \quad (3.4)$$

$$\chi_{\text{sea}} = \frac{\mu(2m_l' + m_h')}{8\pi^2 f_\pi^2}, \quad (3.5)$$

$$\chi_E = \frac{\sqrt{2}E_\pi}{4\pi f_\pi}, \quad \text{and} \quad (3.6)$$

$$\chi_{a^2} = \frac{a^2\bar{\Delta}}{8\pi^2 f_\pi^2}. \quad (3.7)$$

Note that the valence mass m_l is equal to the sea mass m_l' in our data. The low-energy constant μ relates the pseudoscalar meson masses to the quark masses,

$$M_{\xi,\text{PS}}^2 = (m_1 + m_2)\mu + a^2\Delta_\xi, \quad (3.8)$$

and Δ_ξ is the mass splitting for staggered taste ξ. The average taste splitting in Eq. (3.7) is $\bar{\Delta} \equiv \frac{1}{16}\sum_\xi \Delta_\xi$. The quantities μ and Δ_ξ are obtained from the MILC Collaboration's analysis of light pseudoscalar mesons and are shown in Table IX.

We constrain the parameter $g_{B^*B\pi}$ with a prior. The value of $g_{B^*B\pi}$ has been calculated with lattice QCD in the static limit [48,49] or with a relativistic b quark [50] on gauge fields generated with domain-wall or Wilson sea quarks [51]. We set the prior, based on these lattice-QCD calculations, to be $g_{B^*B\pi} = 0.45 \pm 0.08$, where the error covers the differences among different determinations of the

TABLE IX. Fixed parameters that enter the chiral-continuum-extrapolation fit function. The taste splittings $r_1^2 a^2 \Delta_\xi$, $\xi = P, A, T, V, I$ are for the pseudoscalar, axial-vector, tensor, vector, and scalar tastes, respectively. The pseudoscalar taste splittings are zero by virtue of the remnant chiral symmetry of staggered fermions. The hairpin parameters $r_1^2 a^2 \delta_{V(A)}'$ were determined in a combined fit to light-pseudoscalar quantities at multiple lattice spacings. We take the result for these couplings at the $a \approx 0.12$ fm lattice and scale them to other lattice spacings by the ratio $\Delta_{\text{rms}}(a)/\Delta_{\text{rms}}(0.12 \text{ fm})$, where Δ_{rms} is the rooted mean square of the taste splittings. The continuum value of the low-energy constant μ is evaluated at the same scale as the 0.09 fm lattice in our mass-independent scheme.

a (fm)	0.12	0.09	0.06	0.045	0
$r_1^2 a^2 \Delta_P$	0	0	0	0	0
$r_1^2 a^2 \Delta_A$	0.22705	0.07469	0.02635	0.01041	0
$r_1^2 a^2 \Delta_T$	0.36616	0.12378	0.04298	0.01698	0
$r_1^2 a^2 \Delta_V$	0.48026	0.15932	0.05744	0.22692	0
$r_1^2 a^2 \Delta_I$	0.60082	0.22065	0.07039	0.02781	0
$r_1^2 a^2 \delta_V'$	0.0	0.0	0.0	0.0	0
$r_1^2 a^2 \delta_A'$	-0.28	-0.09	-0.03	-0.01	0
$r_1\mu$	6.83190	6.63856	6.48665	6.41743	6.015349

coupling. The LO and NLO coefficients, $\{c_i, 0 \leq i \leq 5\}$, are well determined by the data. Note that the formula given in Eq. (3.1) is slightly different from that in Ref. [5], where the NLO coefficients therein are our $|c_i^J/c_0^J|(i \neq 0)$. With the introduction of variables χ_i defined in Eqs. (3.4)–(3.7), we should expect that $|c_i^J/c_0^J| \lesssim 1(i \neq 0)$, or $|c_i^J| \lesssim |c_0^J|$. In the actual fits, $|c_0^{\perp,\parallel} r_1^{3/2}| \lesssim 0.6$ and $|c_0^T r_1^{3/2}| \lesssim 1.0$. Note that the coefficients c_i^J are dimensionful, and they are evaluated here in r_1 units. We constrain them with loose priors: $c_i^{\perp,\parallel} r_1^{3/2} = 0 \pm 1$ and $c_i^T r_1^{3/2} = 0 \pm 2$.

Standard HMrSχPT uses the assumption that the external and loop pions are soft, i.e., $E_\pi \sim M_\pi$ [52,53]. In our work, however, the external pion energies can be quite large, in some cases as much as 7 times the physical pion mass, and standard HMrSχPT may not converge well enough in this range. Indeed, the fit of the lattice form factor $f_\parallel$ to Eq. (3.1) gives a poor confidence level ($p \sim 0$), which is not improved by including higher-order contributions in the chiral expansion. Bijnens and Jemos [54] proposed an approach called hard-pion χPT, in which the internal energetic pions are integrated out and the E_π dependence is absorbed into the low-energy constants.[2] Since hard-pion χPT provides a more appropriate description of our data, we adopt it in this analysis. The explicit expressions for the hard-pion nonanalytic terms $\delta f_{J,\text{logs}}^{\text{hard}}$ using SU(3) chiral perturbation theory as well as its SU(2) limit are given in the appendix of Ref. [45]. We take the SU(2) limit by integrating out the strange quark. The resulting expression has no explicit strange-quark mass dependence, which has been absorbed into the value of the low-energy constants. The SU(2) hard-pion χPT provides a better description of our $f_\parallel$ data than the SU(3) hard-pion χPT (p value 0.29 versus 0.09 from the NLO χPT fit with priors). We also find that the chiral expansion converges faster using SU(2) χPT when including higher-order chiral corrections in the fit to our data, which results in smaller χPT truncation errors than from using SU(3) χPT. Finally, Ref. [53] provides phenomenological arguments to prefer the application of SU(2) HMχPT over SU(3) to lattice-QCD data. We therefore use the SU(2) formula for our central value fit, but also check the consistency with the SU(3) fits in Sec. IV.

Based on the above discussion, we use the following conditions for $f_\perp, f_\parallel$, and f_T in Eq. (3.1):

$$\delta f_{J,\text{logs}} = \delta f_{J,\text{logs}}^{\text{hard,SU(2)}}, \qquad (3.9)$$

$$\delta D_{\text{logs}} = 0, \qquad (3.10)$$

$$c_2^J = 0, \qquad (3.11)$$

$$\chi_{\text{val}} = \frac{2(2\mu m_l)}{8\pi^2 f_\pi^2} - \frac{a^2 \Delta_I/3}{8\pi^2 f_\pi^2}, \qquad (3.12)$$

where Eq. (3.10) is a consequence of the hard-pion limit, Eq. (3.11) and the factor 2 in the first term of Eq. (3.12) follow from the fact that we take $m_l = m_l'$ and m_h' has been integrated out, Eq. (3.12) preserves the chiral-scale independence of the SU(2) hard-pion NLO expression, and $a^2 \Delta_I$ is the taste splitting of the taste-singlet pseudoscalar meson mass.

The fits of the lattice form factors using NLO SU(2) hard-pion HMrSχPT have acceptable confidence levels. We find, however, that there is a sizable shift in the fit result when including higher-order terms in the χPT expansion. We therefore need to study the effects of higher-order contributions in the chiral expansion.

B. Next-to-next-to-leading-order (NNLO) corrections

We supplement the NLO SU(2) hard-pion χPT expression with the following NNLO analytic terms:

$$\begin{aligned} \delta f_{J,\text{analytic}}^{\text{NNLO}} = {} & c_6^J \chi_{\text{val}} \chi_E + c_7^J \chi_{a^2} \chi_E + c_8^J \chi_E^3 + c_9^J \chi_{\text{val}}^2 \\ & + c_{10}^J \chi_{\text{val}} \chi_E^2 + c_{11}^J \chi_{a^2} \chi_{\text{val}} + c_{12}^J \chi_{a^2} \chi_E^2 \\ & + c_{13}^J \chi_{a^2}^2 + c_{14}^J \chi_E^4, \end{aligned} \qquad (3.13)$$

such that the complete NNLO χPT expression is

$$f_J^{\text{NNLO}} = f_J^{\text{NLO}} + f_J^{(0)} \delta f_{J,\text{analytic}}^{\text{NNLO}}. \qquad (3.14)$$

Note that f_J^{NLO} here uses the hard-pion and SU(2) χPT, as manifested in Eqs. (3.9)–(3.12). All light-quark discretization errors that arise from taste violations are included here; generic errors from light-quark and gluon action, which are $\mathcal{O}(\alpha_s a^2 \Lambda^2)$, are discussed in Sec. III C.

Again, the expectation from chiral perturbation theory is that the coefficients of these analytic terms should satisfy $|c_i^J/c_0^J| \sim \mathcal{O}(1)$ when written in terms of the dimensionless variables χ given in Eqs. (3.4)–(3.7). We set the priors for the NNLO coefficients for $f_{\perp,\parallel}$, $\{c_i^{\perp,\parallel} r_1^{3/2}, 6 \leq i \leq 14\}$, to be 0 ± 0.6, since the role of these terms is simply to absorb the effects of higher-order contributions in the chiral expansion. This width 0.6 corresponds to the size of $|c_0^{\perp,\parallel} r_1^{3/2}|$. For the same reason, we set the priors for the coefficients for f_T, $\{c_i^T r_1^{3/2}, 6 \leq i \leq 14\}$, to be 0 ± 1.0. Doubling the prior widths leads to negligible shifts on the central values of the form factors and less-than-20% increases in the fit errors.

C. Heavy-quark discretization effects

The chiral-continuum extrapolation implemented in Eq. (3.14) accounts for the discretization effects from the gluons and the light staggered quarks. Discretization

---

[2]The factorization of hard-pion χPT breaks down starting at three loops [55], but we only use the one-loop nonanalytic terms.
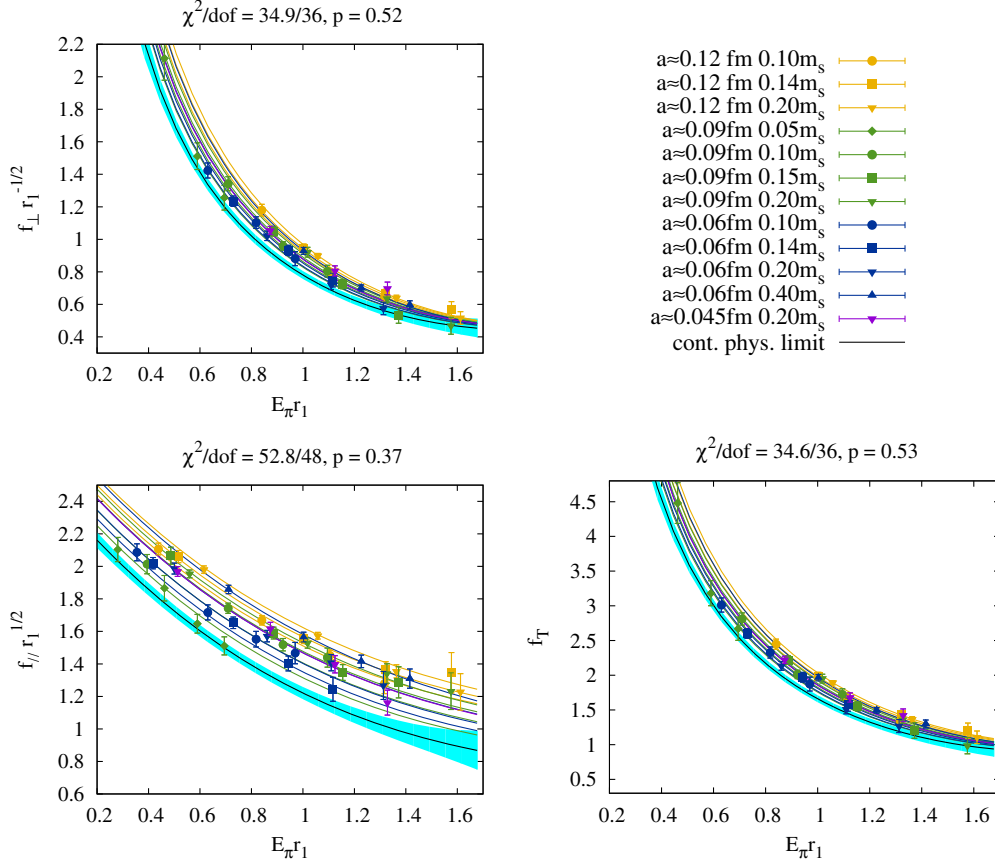
FIG. 11 (color online).   Chiral-continuum extrapolation of lattice form factors $f_\perp$ (upper left), $f_\parallel$ (lower left), and f_T (lower right) as functions of E_π, where all quantities are in r_1 units. The colors denote the lattice spacings: 0.12 fm (gold), 0.09 fm (green), 0.06 fm (blue), and 0.045 fm (violet). The symbols denote the light-quark masses m'_l/m'_h: 0.05 (diamond), 0.1 (circle), 0.15 (square), 0.2 (downward-pointing triangle), and 0.4 (upward-pointing triangle). The colored lines correspond to the fit results evaluated at the parameters of the ensembles. The physical-mass continuum-limit curve is shown as a black curve with cyan error band.

effects from the heavy b quark need a separate treatment. Heavy-quark discretization errors arise from the short-distance mismatch of higher-dimension Lagrangian and current operators [41,42]. By power counting, such mismatches are of $\mathcal{O}(a^2\Lambda^2)$ or $\mathcal{O}(\alpha_s a\Lambda)$ where Λ is a QCD scale appropriate for the heavy-quark expansion. We follow the same method for incorporating the heavy-quark discretization effects described in Ref. [37] and include the following error function in Eq. (3.1):

$$\delta f_J^{HQ} = (z_E^J f_E + z_X^J f_X + z_Y^J f_Y)(a\Lambda)^2$$
$$+ (z_B^J f_B + z_3^J f_3)(\alpha_s a\Lambda) + z_0^J \alpha_s (a\Lambda)^2, \quad (3.15)$$

where the mismatch functions $f_{E,X,Y,B,3}$ are given in the appendix of Ref. [37]. The error functions $f_{B,E}$ arise from mismatches of operators in the Lagrangian, while functions $f_{X,Y,3}$ arise from those of the vector current. The last term in Eq. (3.15) accounts for higher-order heavy-quark and generic light-quark and gluon errors not included in Eq. (3.14), which is of the order $\alpha_s(a\Lambda)^2$. The fit

parameters are constrained with priors: 0 ± 1 for z_Y, z_B, z_0 and $0 \pm \sqrt{2}$ for z_X, z_3; the latter two are wider because the functions f_X and f_3 both appear twice [42].

To summarize, after incorporating the heavy-quark discretization effects, the complete NNLO SU(2) hard-pion HMrSχPT expression is

$$f_J^{NNLO+HQ} = f_J^{NNLO} \times (1 + \delta f_J^{HQ}), \quad (3.16)$$

where f_J^{NNLO} is defined in Eq. (3.14). With this treatment, the uncertainty due to truncating the chiral expansion at NNLO (cf. Sec. IV below), NNLO light-quark and gluon discretization effects, and LO heavy-quark discretization effects are incorporated in the fit error of the chiral-continuum extrapolation. The fits for $f_\perp$, $f_\parallel$, and f_T to Eq. (3.16) are shown in Fig. 11.

To examine the size of discretization effects, we plot the form factors $f_\perp$ and $f_\parallel$ with light-quark mass $m'_l = 0.2m'_h$ at each lattice spacing versus a^2 in Fig. 12. As we can see from the plots, the observed lattice-spacing dependence is very mild, with the data points at the largest lattice spacing
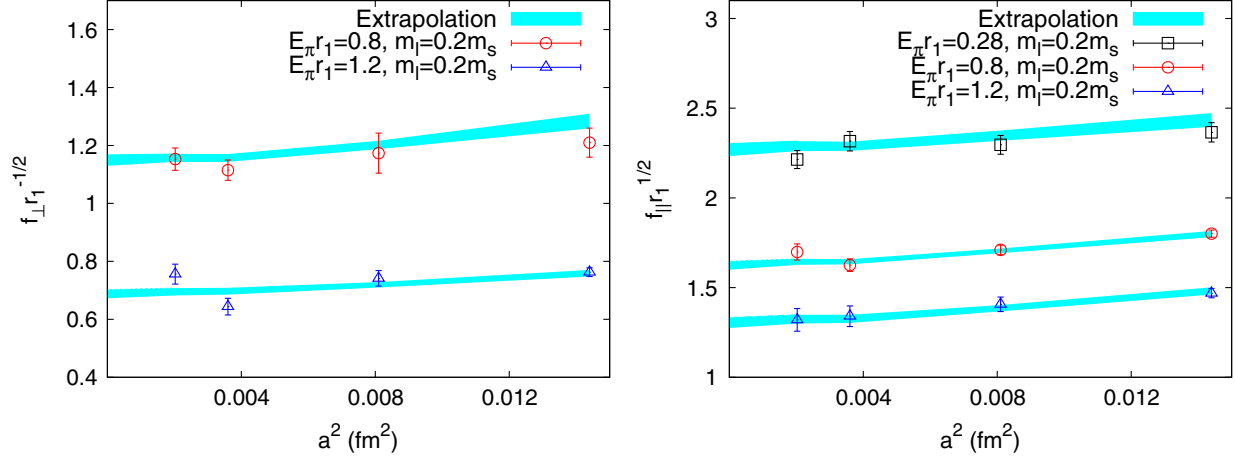
FIG. 12 (color online).   Discretization effects in the form factor $f_\perp$ (left) and $f_\parallel$ (right) at a few kinematic points. The plots show the form factors on the $m'_l = 0.2m'_h$ ensembles at each lattice spacing versus a^2 for various pion momenta (a slight extrapolation/interpolation is applied to adjust the raw data to the same $E_\pi r_1$). The range $E_\pi r_1 \in [0.28, 1.2]$ is used in the q^2 extrapolation to the full kinematic range.

($a \approx 0.12$ fm) only about two statistical σ away from the continuum limit.

IV. SYSTEMATIC ERROR BUDGET

The error output from the central-value fit described in Sec. III C already includes the systematic errors due to the light- and heavy-quark discretization effects and the uncertainty on $g_{B^*B\pi}$. We now discuss other sources of systematic uncertainty. We tabulate systematic error budgets for f_+ and f_0 at a representative kinematic point $q^2 = 20$ GeV^2 within the range of lattice data in Table X. We also present the error budget for the full simulated lattice momentum range in Fig. 17.

A. Chiral-continuum extrapolation

As discussed above, our central fit uses NNLO[3] SU(2) hard-pion HMrSχPT including contributions from heavy-quark discretization effects and the uncertainty in $g_{B^*B\pi}$. Here we consider variations of the fit function and the data included to estimate truncation and other systematic effects.

First, we study the effects of truncating the chiral expansion by adding next-to-NNLO (NNNLO) analytic terms $\delta f^{\rm NNNLO}_{J,\text{analytic}}$ in our fits with coefficients constrained with the same priors as the NNLO coefficients. The variations in f_+ due to changing the order of the χPT analytic terms are shown in Fig. 13. The fits of different orders are consistent in the q^2 region where most of the simulation data are located. Although the central values and errors differ noticeably between the NLO and NNLO fits, the central values and errors of the NNNLO fit are very close to the NNLO fit, indicating that the chiral extrapolation has stabilized by NNLO. As discussed earlier, the

---

[3]NLO + NNLO analytic terms.

NLO coefficients are well determined by the data, and we use well-motivated priors based on expectations from χPT for the NNLO and higher-order terms. The fact that the error saturates with NNLO shows that the preferred fit already incorporates the uncertainty from truncating the chiral expansion, and that we do not need to add an additional systematic error. The NNLO fit error as a function of q^2 is shown in Fig. 14.

The standard soft-pion HMrSχPT fits of $f_\perp$ have reasonable confidence levels, but those of $f_\parallel$ do not. Here we estimate the effect of using the hard-pion formalism by using standard HMrSχPT for $f_\perp$ but still employing hard-pion χPT for $f_\parallel$. The resulting difference from the preferred fit is small, less than 1% for f_+. The same conclusion also holds for the form factor f_0.

We use SU(2) χPT, instead of SU(3) χPT, for our central fit. To estimate the effect of this choice, we restore the strange-quark dependence of the logarithm and analytic terms in Eq. (3.1). A practical issue arises with NNLO SU(3) χPT, where the terms proportional to the sea-quark mass, $\chi_{\rm sea}$, are not well constrained by our data because the strange sea-quark mass m'_h is so similar on all of our

TABLE X.   Error budgets of form factors f_+ and f_0 at $q^2 = 20$ GeV^2.

| Uncertainty	δf_+	δf_0
Statistical + χPT + HQ + $g_{B^*B\pi}$	3.1	3.8
Scale r_1	0.5	0.7
Nonperturbative $Z_{V^4_{bb}}$	0.4	0.6
Nonperturbative $Z_{V^4_{ll}}$	0.4	0.4
Perturbative ρ	1.0	1.0
Heavy-quark mass mistuning	0.4	0.4
Light-quark mass tuning	0.4	0.2
Total	3.4	4.1
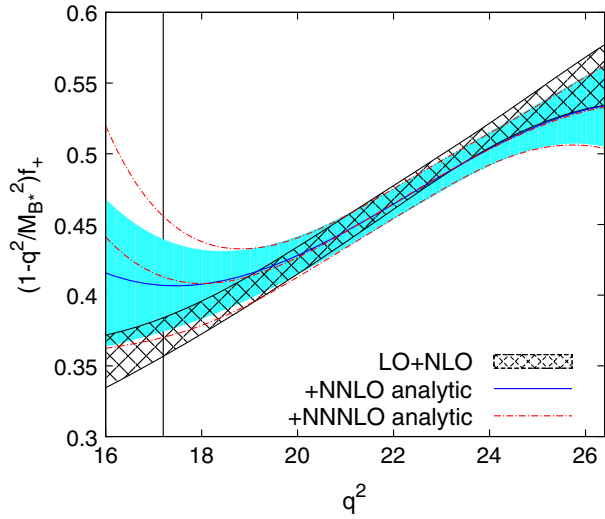
FIG. 13 (color online). The function $(1 - q^2/M_{B^*}^2)f_+$ obtained from the chiral-continuum fits with NLO logarithms and analytic terms through NLO (hatched black band), NNLO (solid cyan band) and NNNLO (dashed red lines). Errors shown are fit statistical errors only. The vertical line indicates the lowest q^2 of the lattice data.

ensembles. To obtain some sensitivity to χ_{sea}, we include data on an additional $a \approx 0.12$ fm ensemble with an unphysically small strange-quark mass, $am'_{h,\text{sea}} = am'_{l,\text{sea}} = 0.005$. With the inclusion of this ensemble, we find the fit parameters for the terms involving χ_{sea} are better constrained. The differences between the NNLO SU(3) fits and the preferred fits are shown in Fig. 14. For f_+, the difference is within the statistical error. For f_0, the difference lies outside the statistical error for some of the simulated q^2 range, but the NNLO SU(3) fit quality is poor, with a p-value of 0.01. Because SU(3) χPT does not provide a good description of our data for f_0, we do not

take the difference between NNLO SU(2) and SU(3) fits as a systematic error.

To check how our results are affected by data with high momenta, we also perform a fit excluding data with $\boldsymbol{p} = (2\pi/L)(1, 1, 1)$. As shown in Fig. 14, the form factors f_+ and f_0 from the low-momentum fit agree very well with those from the preferred full-data fit for the region $q^2 > 20$ GeV^2. The systematic difference increases for small q^2, where the highest-momentum data provide important information.

Figure 14 summarizes the effects of all these variations. Comparing the deviations between the central values of the alternate and preferred fits to the statistical error of the preferred fit, we find that the deviations are almost always smaller than the statistical error of our preferred fit. This confirms that fit errors of our preferred fits adequately account for the systematic effects associated with these variations. We therefore do not quote any additional systematic error due to these sources.

We include heavy-quark discretization effects in our chiral-continuum extrapolation. As a consistency check, we compare our result with a power-counting estimate obtained by evaluating δf_J^{HQ} in Eq. (3.15) at the $a \approx 0.045$ fm lattice spacing, setting the coefficients $z_i = 1$ and taking $\Lambda = 500$ MeV for the heavy-quark scale. We find $\delta f_J^{\text{HQ}} \simeq 1.5\%$. Figure 15 shows that the NNLO fit error (without the heavy-quark discretization effects) added to the 1.5% power-counting estimate in quadrature yields a similar error to that of the full fit. Thus, again, it is not necessary to add an additional error to that of the preferred chiral-continuum fit.

B. Light- and bottom-quark mass uncertainties

The effect of mistuning the b-quark mass in our simulation has been largely reduced via the corrections
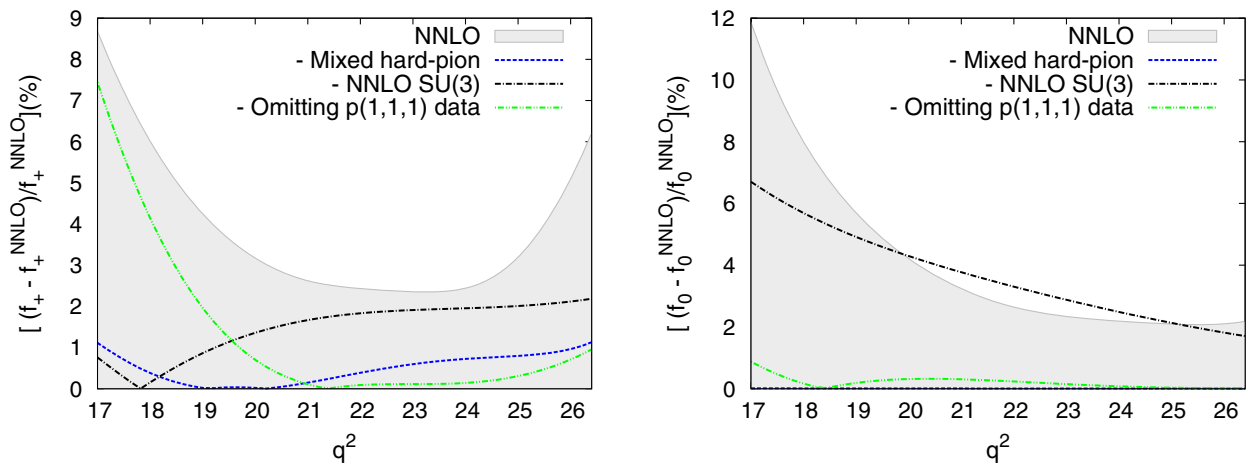

FIG. 14 (color online). Variations in the chiral-continuum extrapolation from different fit *Ansätze*. The shaded area shows the fit error from the preferred NNLO SU(2) fit. The other curves show the systematic deviations from the NNLO SU(2) fit under the variations discussed in the text.
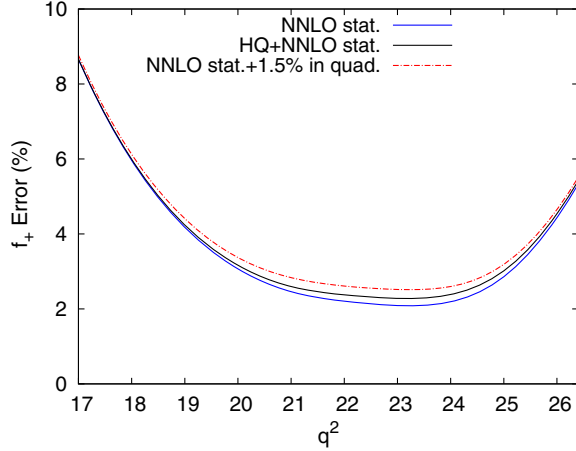
FIG. 15 (color online). Heavy-quark discretization effects in the chiral-continuum fit. The solid blue, solid black, and dashed red curves show the NNLO fit error, the preferred fit error, and the NNLO fit error added to a 1.5% power-counting estimate of heavy-quark discretization errors, respectively.

described in Sec. II F. Errors still arise, however, from the uncertainty in the tuned value κ_b itself and from the procedure for shifting the form factors. From Eq. (2.30) we estimate the relative error by

$$\frac{\delta f}{f} \approx \left(\frac{\partial \ln f}{\partial \ln \bar{m}_2} \right) \frac{\delta(1/m_2)}{1/m_2} + \delta\left(\frac{\partial \ln f}{\partial \ln \bar{m}_2} \right) \frac{1/m_2 - 1/\bar{m}_2}{1/\bar{m}_2},$$
(4.1)

where $\delta(1/m_2)$ is related to the uncertainty due to the error in κ_b, while $\delta\left(\frac{\partial \ln f}{\partial \ln \bar{m}_2}\right)$ is the uncertainty on the normalized slope. The values of the physical κ_b with errors are given in Table VII, and we can find the statistical uncertainty of the normalized slope using Table VIII. Using Eq. (2.30), we find that the value of $\delta f/f$ on all ensembles is at most 0.6%. We take the average value for $\delta f/f$ on all ensembles, which is 0.4%, to be the error due to tuning κ_b, and assign the same error to f_+ and f_0.

To obtain the physical form factors, we evaluate the result of the chiral-continuum fit at the physical light- and strange-quark masses determined from the MILC Collaboration's analysis of light pseudoscalar mesons [19]. (Although we use SU(2) χPT, we include an analytic term proportional to χ_{sea} to allow for a slight shift to the physical strange sea-quark mass.) The errors on the physical $m_l \equiv (m_u + m_d)/2$ and m_s are 3.5% and 3.0%, respectively. We vary the light- and strange-quark masses at which the chiral-continuum fit function is evaluated by plus and minus one standard deviation, and find that it produces differences below 0.4% in both form factors.

C. Lattice scale r_1

We convert the lattice form factors and pion energies to physical units using the relative scale r_1/a determined from

the static-quark potential (see Table III) and the absolute scale $r_1 = 0.3117(22)$ fm [37]. The statistical uncertainties on r_1/a are negligible. We propagate the uncertainty in r_1 by shifting it $\pm 1\sigma$ and repeating the chiral-continuum fit. We find shifts of at most 0.7% in the range of simulated momenta.

D. Current renormalization

With the mostly nonperturbative renormalization procedure that we use for the heavy-light currents, there are two sources of error. The first is due to the nonperturbatively calculated flavor diagonal factors $Z_{V^4_{bb}}$ and $Z_{V^4_{ll}}$. Their values and errors are given in Table VI. We estimate the systematic error due to the uncertainties of $Z_{V^4_{bb}}$ and $Z_{V^4_{ll}}$ by varying their values by one σ and looking for the maximum deviations in the form factors f_+ and f_0. The resulting deviations are small, ranging from 0.4% to 0.6%.

The second source of error is due to the truncation of the perturbative expansion in the calculation of the ρ_J's. Because the ρ_J's are defined from ratios of renormalization constants, their perturbative corrections are small by construction. Indeed, as seen in Table VI, for V^4_{bl} they are less than 1% and for V^i_{bl} they range between 2% and 3%. For the scale-independent vector current, we observe that the one-loop corrections to $\rho_{V^4_{bl}}$ are smaller than those for $\rho_{V^i_{bl}}$, and we use the same error estimate for both. In order to accommodate possible accidental cancellations, we take the error as $2\rho^{[1]}_{\max}\alpha_s^2$, where $\rho^{[1]}_{\max}\alpha_s$ is an upper bound of the one-loop correction to V^μ_{bl} in the range of heavy-quark mass $am_0 \leq 3$ that corresponds to the range of lattice spacings included in our analysis. The coupling is evaluated at the scale of the next-to-finest lattice spacing in our calculation, $a \approx 0.06$ fm. This procedure yields an error estimate of 1%, which is larger than the one-loop correction to $\rho_{V^4_{bl}}$ over most of the mass range, and amounts to about 50% of the one-loop correction to $\rho_{V^i_{bl}}$ in the mass range that corresponds to the three finest lattice spacings. This leads to an error of 1% for both f_+ and f_0 due to the perturbative renormalization factors.

E. Finite-volume effects

We estimate the size of the finite-volume effects by replacing the infinite-volume chiral logarithms with discrete sums and repeating the chiral-continuum extrapolation. The change in our preferred fit after including finite-volume corrections is very small, less than 0.01%, which we simply neglect.

F. Summary

Figures 16 and 17 visually summarize the systematic error budget for the vector and scalar form factors f_+, f_0 in the simulated lattice-QCD momentum range. By far the largest contribution to the total uncertainty is from the fit
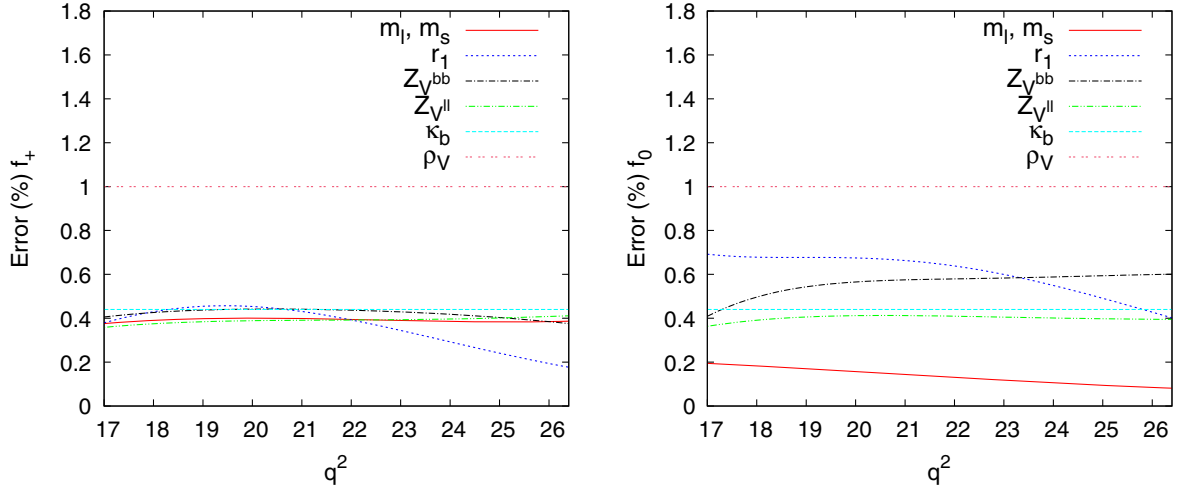
FIG. 16 (color online). Subdominant systematic errors over the range of simulated lattice momenta. Error estimates are described in the text.

error, which includes the statistical uncertainty in addition to the chiral-continuum extrapolation and heavy-quark discretization errors. The total error on f_+ is smallest, about 3%, in the region of $q^2 \approx 20$–24 GeV^2.

The subdominant errors, such as those from heavy-quark mass tuning, the current renormalization, etc., have mild q^2 dependence, as can be seen in Fig. 16. We therefore treat them as constant in q^2 when propagating them. For each source, we take the maximum estimated error in the simulated q^2 range; we then add these individual error estimates in quadrature to obtain an overall additional systematic error δ_f. We find $\delta_{f_+} = 1.4\%$ and $\delta_{f_0} = 1.5\%$.

In the next section, we will use our result for f_+ to obtain $|V_{ub}|$ via a combined fit with experimental data to the z expansion. Due to phase-space suppression, the

experiments have poor access to the large-q^2 region. On the other hand, the lattice-QCD form factor has a larger error than experiment at small q^2 due to the sizable q^2 extrapolation. As discussed below, the value of $|V_{ub}|$ is mostly determined in the region $q^2 \approx 20$ GeV^2, which is at the low end of the q^2 range where the lattice-QCD form-factor error is still small. We therefore provide tabulated error budgets for the two form factors f_+, f_0 from our calculation at the particular kinematic point $q^2 = 20$ GeV^2 in Table X. The error on $f_+(20$ GeV$^2)$ is approximately 3.4%, which is about one third of the error on our previously determined form factor in Ref. [5].

We compare our results for f_+ and f_0 with full errors, which are obtained by adding the fit errors from the χPT fits and δ_f in quadrature, with previous lattice-QCD
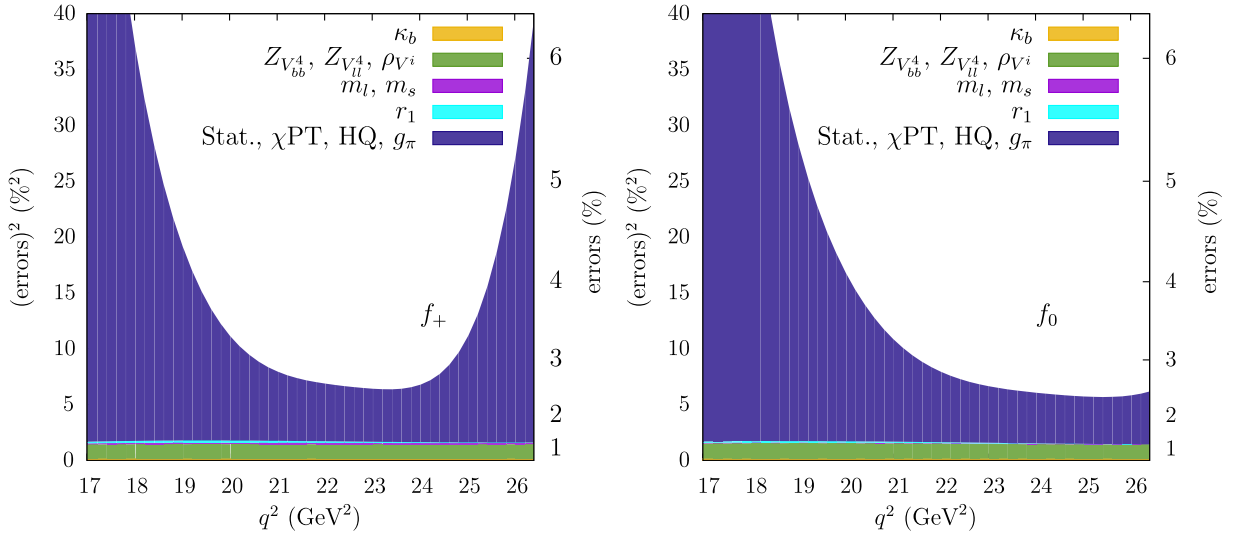
FIG. 17 (color online). The distribution of the errors for f_+ (left) and f_0 (right) as a function of q^2. The different bands in the plot show the contribution of the error source to the sum of squared errors (left y axis). The corresponding error can be read off from the right y axis.
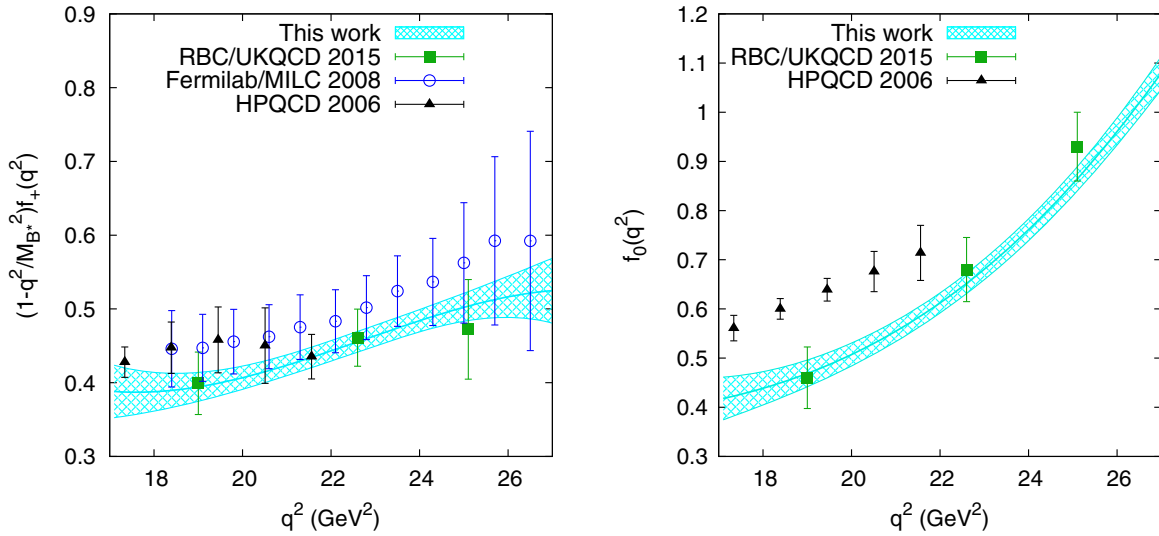
FIG. 18 (color online). Comparison of f_+ (left) and f_0 (right) from this work with previous lattice-QCD calculations by HPQCD [4], Fermilab/MILC [5], and RBC/UKQCD [13].

calculations in Fig. 18. Our result for f_+ agrees with previous results obtained at $q^2 \gtrsim 17$ GeV^2 from Refs. [4,5,13], but is more precise. Our result for f_0 is consistent with Ref. [13], but not with Ref. [4].

V. z EXPANSION AND DETERMINATION OF $|V_{ub}|$

The chiral-continuum extrapolation described in the previous sections yields the form factors in the range 17 GeV$^2 \leq q^2 \leq 26$ GeV^2. In this section, we extrapolate them to the full kinematic range using the model-independent z expansion. The form factors resulting from the chiral-continuum extrapolation are functions specified by a set of parameters. One could, in principle, incorporate the z expansion with the χPT expansion from the outset (see, e.g., Ref. [56]). With such an approach, however, the coefficients of the z expansion will have a nontrivial dependence on m_l and a that must be derived from the underlying chiral effective theory. Because the dependence of the coefficients on a and m_l is unknown, we instead carry out the extrapolation in two steps, taking the chiral-continuum-extrapolated results and feeding them into the z expansion. We introduce a functional method to perform the z expansion. We also apply the z expansion to the experimental data and, after verifying that the fits to experiment and to lattice QCD are consistent, we carry out a combined fit to obtain $|V_{ub}|$. A byproduct of the last step is a precise determination for $f_+(q^2)$ constrained by lattice QCD at high q^2 and experiment at low q^2.

A. z expansions of heavy-light semileptonic form factors

The z expansion involves mapping the variable q^2 to a new variable z by [57]

$$z(t, t_0) = \frac{\sqrt{t_+ - q^2} - \sqrt{t_+ - t_0}}{\sqrt{t_+ - q^2} + \sqrt{t_+ - t_0}}, \qquad (5.1)$$

where $t_{\pm} = (M_B \pm M_{\pi})^2$, and t_0 is chosen for convenience below. This change of variables maps the whole complex q^2 plane onto the unit disk in the z plane, where the upper (lower) path along the branch cut $[t_+, \infty)$ is mapped to the lower (upper) half of the circle enclosing the unit disk in the complex z plane. Choosing $t_0 = (M_B + M_{\pi})(\sqrt{M_B} - \sqrt{M_{\pi}})^2$ centers the full kinematic range for semileptonic $B \to \pi \ell \nu$ decay around the origin $z = 0$ and, moreover, restricts z to $|z| < 0.28$. The small, bounded interval, together with a constraint from unitarity ensures convergence of the expansion. As discussed below, we find in practice that the convergence is rapid.

The form factors f_+ and f_0 are analytic in z except for the branch cut $[t_+, \infty)$ and poles in $[t_-, t_+]$. We can write

$$P_i(z)\phi_i(z)f_i = \sum_n a_n z^n, \qquad (5.2)$$

where $P_i(z)$; $i = +, 0$, are the Blaschke factors, which are introduced to remove the poles of f_i in the region $[t_-, t_+]$; and $\phi_i(z)$ are the outer functions [57,58]. We choose simple outer functions $\phi_{+,0} = 1$ and employ the following formulas to expand the form factors:

$$f_+(z) = \frac{1}{1 - q^2(z)/M_{B^*}^2} \sum_{n=0}^{N_z - 1} b_j^+ \left[z^n - (-1)^{n-N_z} \frac{n}{N_z} z^{N_z} \right],$$
$$(5.3)$$

$$f_0(z) = \sum_{n=0}^{N_z} b_n^0 z^n. \qquad (5.4)$$

TABLE XI. The BCL constants used to estimate $\Sigma(b, N_z)$.

	B_{00}	B_{01}	B_{02}	B_{03}	B_{04}	B_{05}	B_{06}
f_0	0.1032	0.0408	−0.0357	−0.0394	−0.0195	−0.0055	−0.0004
f_+	0.0198	0.0042	−0.0109	−0.0059	−0.0002	0.0012	0.0011

Equation (5.3) is known as the Bourrely-Caprini-Lellouch (BCL) expansion [59], which is constructed to reproduce the threshold behavior at $q^2 = t_+$ and the asymptotic behavior as $q^2 \to \pm\infty$. Equation (5.4) is a simple series expansion of f_0 in z.

The BCL coefficients in Eqs. (5.3) and (5.4) obey the unitarity constraint [57,59]

$$\Sigma(b, N_z) \equiv \sum_{m,n=0}^{N_z} B_{mn} b_m b_n \lesssim 1, \qquad (5.5)$$

where the element B_{mn} satisfies $B_{nm} = B_{mn} = B_{0|m-n|}$ and depends on the choice of t_0 [59]. We tabulate the values of B_{0k} for the form factors f_+, f_0 in Table XI. The inequality saturates when $N_z \to \infty$. Although we do not incorporate this constraint into our fits, we check that our results satisfy it.

B. Functional method for the z expansion

In previous work, we have used synthetic data points generated from the χPT fit as inputs to the z fit [5], but here we take a new approach. We exploit the facts that the χPT expansion is linear in the fit parameters and that it contains only a finite number of independent functions [see Eq. (3.1)]. We construct a covariance function $K(z_1, z_2)$, defined as the covariance of any pair of points (z_1, z_2), using the set of functionals from the χPT expansion. Our new approach is to formulate the z expansion using the eigenfunctions of an integral operator defined from $K(z_1, z_2)$.

Let us start with the NLO χPT expression Eq. (3.1), as an example. Because $f_\perp$ and $f_\parallel$ are linear in their coefficients $c_i^\perp$ and $c_i^\parallel$, we can express them both in the compact form

$$f_J(m_\ell, m_s, a^2, E_\pi) = C_J \cdot X_J, \qquad (5.6)$$

where

$$C_J \equiv [c_0 \quad c_1 \quad c_2 \quad c_3 \quad c_4 \quad c_5 \quad \ldots]^J, \qquad (5.7)$$

$$X_J \equiv f_J^{(0)}[(1 + \delta f_{J,\text{logs}}) \quad \chi_{\text{val}} \quad \chi_{\text{sea}} \quad \chi_E \quad \chi_E^2 \quad \chi_{a^2} \quad \ldots]^T, \qquad (5.8)$$

and where $J = \perp, \parallel$ and the variables are defined in Eqs. (3.4)–(3.6). Any linear combination of $f_\perp$ and $f_\parallel$ can be written as

$$f = [\xi \quad \eta] \begin{bmatrix} f_\perp \\ f_\parallel \end{bmatrix} = [C_\perp^T \quad C_\parallel^T] \begin{bmatrix} \xi X_\perp \\ \eta X_\parallel \end{bmatrix}, \qquad (5.9)$$

with ξ, η functions of q^2. The uncertainty of the function f is encoded in the uncertainty in the coefficient vector C_J. In all these expressions, we are only interested in the terms with E_π (or q^2) dependence and, hence, z dependence. We can now define the covariance function $K(z, z')$ in some valid domain $[z_1, z_2]$. Explicitly,

$$K(z, z') = Y(z)^T \cdot \text{Cov} \cdot Y(z'), \qquad (5.10)$$

where

$$Y(z) = \begin{pmatrix} \xi(z) X_\perp(z) \\ \eta(z) X_\parallel(z) \end{pmatrix}, \qquad (5.11)$$

and Cov is the covariance matrix of the involved coefficients c_n^J:

$$\text{Cov}_{mn} = \langle \delta c_m \delta c_n \rangle. \qquad (5.12)$$

The covariance function $K(z, z')$ is a Mercer kernel [60], and Mercer's theorem ensures that there exists a set of orthonormal functions $\psi_i(z)$ defined over the domain $[z_1, z_2]$ such that

$$K(z, z') = \sum_i \lambda_i \psi_i(z) \psi_i(z'), \qquad (5.13)$$

where λ_i, ψ_i are the eigenvalues and eigenfunctions of the operator L_K induced by the integral equation

$$L_K \psi(z) = \int_{z_1}^{z_2} K(z, z') \psi(z') dz'. \qquad (5.14)$$

The form factor $f(z)$ can naturally be expanded in the basis of $\psi_i(z)$: we only need to project the expansions in Eqs. (5.3) and (5.4) onto the same basis. The process of finding the expansion coefficients b_n is equivalent to minimizing the following function (in analogy to the usual χ^2 function, replacing the sum over discrete points with an integral over a continuous variable):

$$\chi_{\text{lat}}^2 = \int_{z_1}^{z_2} dz \int_{z_1}^{z_2} dz' [f^{\chi\text{PT}}(z) - g_f(b, z)] K^{-1}(z, z')$$
$$\times [f^{\chi\text{PT}}(z') - g_f(b, z')]$$
$$= \sum_{i=1}^{N_\psi} \frac{1}{\lambda_i} \left[\int_{z_1}^{z_2} dz [f^{\chi\text{PT}}(z) - g_f(b, z)] \psi_i(z) \right]^2$$
$$= \sum_{i=1}^{N_\psi} \frac{1}{\lambda_i} \left[f_i^{\chi\text{PT}} - \sum_{n=0}^{N_z-1} b_n \int_{z_1}^{z_2} \theta_n^f(z) \psi_i(z) dz \right]^2, \qquad (5.15)$$

where

$$f^{\chi\text{PT}}(z) = \sum_i f_i^{\chi\text{PT}} \psi_i(z) \tag{5.16}$$

is the form-factor function from the χPT fit expanded in terms of ψ_i, and

$$g_f(b, z) = \sum_{n=0}^{N_z - 1} b_n \theta_n^f(z) \tag{5.17}$$

are functions rewritten from the functions defined in Eqs. (5.3) and (5.4). For brevity, we define

$$\theta_n^+(z) = \frac{1}{1 - q^2(z)/M_{B^*}^2} \left[z^n - (-1)^{n - N_z} \frac{n}{N_z} z^{N_z} \right], \tag{5.18}$$

$$\theta_n^0(z) = z^n. \tag{5.19}$$

To summarize, we expand any form-factor function $f^{\chi\text{PT}}$ obtained from the chiral-continuum extrapolation in the basis formed by the eigenfunctions of its covariance function $K(z, z')$. We then project the z expansion onto the same basis. Finally, we solve for the expansion parameters b_n by minimizing the function χ_{lat}^2 defined in Eq. (5.15).

C. Details on z expansion of the form factors

In addition to the fit errors from the chiral-continuum fit, we also need to propagate the subdominant errors, which have very mild q^2 dependence. We treat them as constant in q^2 and add them in quadrature, obtaining $\delta_{f_+} = 1.4\%$ and $\delta_{f_0} = 1.5\%$. To include this effective subdominant error to the fit, we slightly modify the covariance function defined in Eq. (5.10) by

$$K'(z, z') = Y(z)^T \cdot \text{Cov}' \cdot Y(z'), \tag{5.20}$$

where the new covariance matrix includes the subdominant error,

$$\text{Cov}'_{mn} = \langle \delta c_m \delta c_n \rangle + \delta_f^2 c_m c_n. \tag{5.21}$$

In the function array $Y(z)$ defined in Eq. (5.11), only a relatively small number of the elements are independent functions. For example, there are 42 terms in the NNLO SU (2) χPT fit functions for $f_{\parallel,\perp}$ (including the HQ discretization contributions). Many of them, however, are set to zero in the continuum limit or become constant once the light-quark mass is fixed at its physical value. In the end, the chiral-continuum extrapolated f_+ is described by only six independent functions. For f_0, the number of independent functions is seven. Although we work in the functional basis in which the covariance function $K(z, z')$ is
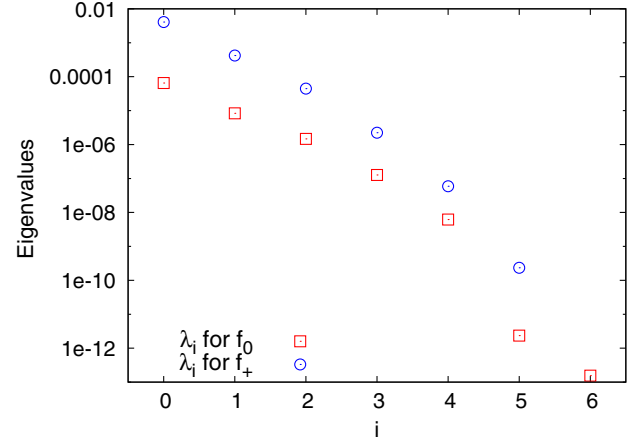
FIG. 19 (color online). Eigenspectrum of the kernel function $K(z, z')$ for f_0 and f_+.

diagonalized, singular modes can arise because $K(z, z')$ is built upon Cov_f, which itself may have singular modes. Figure 19 shows the spectra of the operator L_K for form factors $f_{+,0}$. The spectrum of f_0 contains two very small eigenvalues $\lesssim 10^{-12}$, and they are well separated from the other modes. When we discard these two modes, the fit quality of the functional z fit improves from $p = 0.03$ to $p = 0.46$. For f_+, we do not need to apply any cut on the eigenvalues.

We first consider separate fits of f_+ and f_0 without any constraints on the coefficients of the z expansion. With $N_z = 3$, or three free parameters b_0, b_1, b_2, we obtain a low confidence level, $p = 0.05$, for the fit to f_0. The analogous three-parameter fit for f_+ results in an acceptable confidence level, $p = 0.3$. With $N_z = 4$, we find good confidence levels for both form factors as well as sizable changes in the central values and errors (compared to the $N_z = 3$ case). The results of unconstrained fits of f_+ and f_0 with several values of N_z for f_0 and f_+ are given for comparison in Table XII. The kinematic constraint $f_+(q^2 = 0) = f_0(q^2 = 0)$ is satisfied automatically, as is shown in Fig. 20 (left).

The z-expansion coefficients b_i should approximately satisfy the unitarity bound Eq. (5.5). Figure 21 (right) shows the bootstrap-sample distribution of $\Sigma(b, 4)$ from the fits for f_0. The unitarity condition is marginally satisfied. In the case of f_+, the sum $\Sigma(b, 4) \sim 0.03$ is much smaller than the unitarity bound. Reference [61] pointed out that the smallness is expected based on heavy-quark physics. The value of $\Sigma(b, 4)$ should be of order $(\Lambda/m_b)^3$, which is about 0.013 with a conservative choice of $\Lambda = 1$ GeV. The bootstrap-sample distribution of $\Sigma(b, 4)$ from the fits for f_+ is shown against the heavy-quark estimate in Fig. 21 (left). They are consistent with each other.

The results of the fits of $f_{+,0}$ with the kinematic constraint are shown in Fig. 20 (right). With this constraint, we again examine how the fit varies with higher-order N_z.

TABLE XII.　Results from unconstrained z fits of f_0 and f_+.

N_z	f_+			f_0	
	3	4	5	3	4
$\chi^2/$d.o.f.	1.1	1.0	1.6	3.1	0.54
d.o.f.	3	2	1	2	1
p	0.27	0.33	0.2	0.05	0.46
$\sum B_{mn}b_m b_n$	0.052(16)	0.024(39)	2(4)	0.60(24)	2.0(11)
$f(0)$	0.12(6)	0.23(20)	0.40(34)	$-0.14(9)$	0.20(17)
b_0	0.409(16)	0.409(12)	0.407(15)	0.493(22)	0.510(23)
b_1	$-0.72(13)$	$-0.63(20)$	$-0.60(22)$	$-2.1(2)$	$-1.7(2)$
b_2	$-1.0(2)$	$-0.3(1.3)$	0.3(1.7)	$-0.8(5)$	1.2(9)
b_3		1(2)	4(5)		3(1)
b_4			7(7)		

We find that the fit central values do not change significantly when we change N_z from 4 to 5, in contrast to the case from 3 to 4, as is shown in Fig. 22 and Table XIII.

We perform several additional checks to confirm the stability of our results against various fit choices. In our preferred fit, we set the integral range in Eq. (5.15) to be $z = [-0.25, 0.01]$ (or equivalently $q^2 = [19.8, 26.0]$). The results, however, do not change noticeably if we extend the integral range to $z = [-0.249, 0.069]$, which covers the full range of simulated lattice momenta. This is because the statistical fluctuations and correlations of the form-factor functions are largely decided by the region $-0.1 \lesssim z \lesssim 0$, where the χPT fit results are the most precise.

We also try removing the smallest eigenvalue from the covariance function $K(z, z')$ for f_+; we find that the resulting central values are essentially unaffected. Finally, we also try the fit using, instead of the BCL formula, the Boyd-Grinstein-Lebed (BGL) formula, which uses more complicated outer functions [58]. We find that the resulting form factors are within one standard deviation of the BCL result.

To summarize, we obtain our preferred result from a simultaneous fit to f_+ and f_0 with $N_z = 4$ and with imposing the kinematic constraint $f_+(q^2 = 0) = f_0(q^2 = 0)$. The results for the two form factors f_+ and f_0 are plotted in Fig. 23. In this plot, the form factors obtained from the χPT fit are overlaid on the results of the z fit. The z fit faithfully reproduces the χPT fits in the region where χPT is reliable (indicated by the ranges of the hatched bands). The z coefficients with errors from our preferred fit and their correlation matrix are provided in Table XIV. This information is sufficient to reproduce the lattice form-factor results over the full kinematic range.

Figure 24 shows a comparison of our results with other theoretical calculations of the form factors [13,62]. While our results are consistent with the previous results, ours are significantly more precise in the region of $z \leq 0.1$.

Finally, it is interesting to compare the lattice form factors with theoretical expectations from heavy-quark symmetry. In the soft-pion limit, the vector and scalar form factors f_+ and f_0 are related as [63]
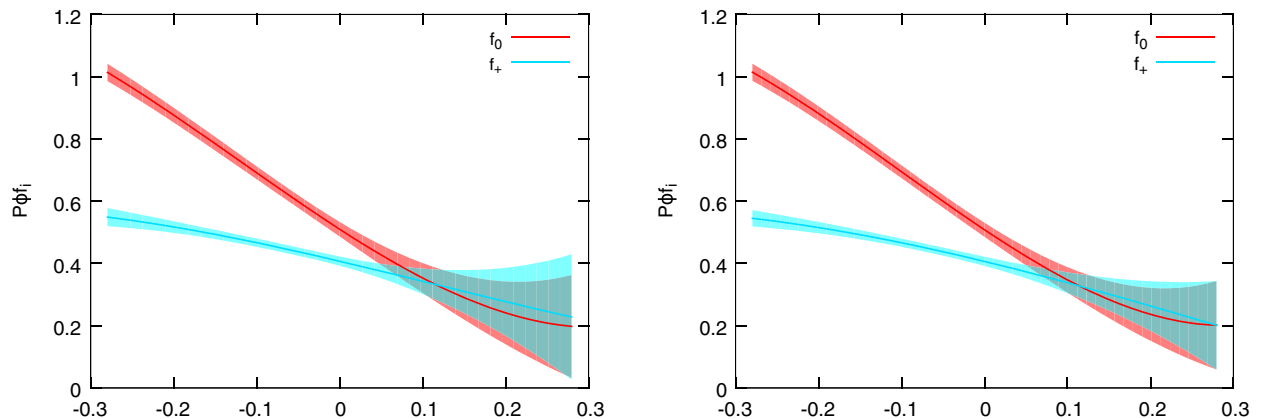

FIG. 20 (color online).　The z expansion of the form factors f_+ and f_0 without any constraints (left) and with the kinematic constraint. The fits use $N_z = 4$.
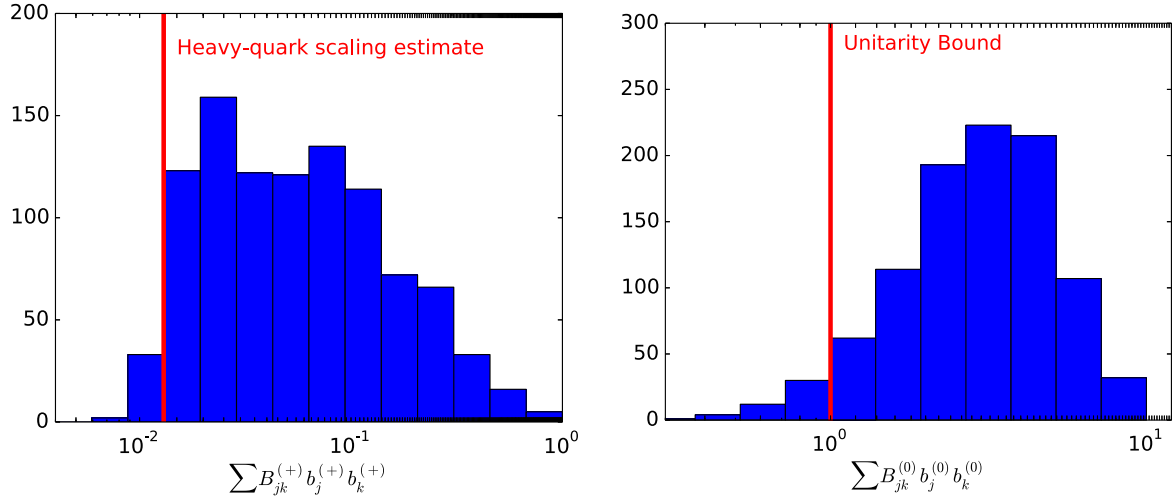
FIG. 21 (color online). Bootstrap-sample distribution defined in Eq. (5.5) for the z-expansion coefficients of f_+ (left) and f_0 (right), compared with the heavy-quark scaling estimate 0.013 (red vertical line in the left plot) and the unitarity bound (red vertical line in the right plot). The 1000 samples of fits use only the kinematic constraint and $N_z = 4$.

$$\lim_{q^2 \to M_B^2} \frac{f_0(q^2)}{f_+(q^2)} = \left(\frac{f_B}{f_{B^*}}\right) \frac{1 - q^2/M_{B^*}^2}{g_{B^* B \pi}} \qquad (5.22)$$

up to corrections of $\mathcal{O}(1/m_b^2)$. This expression updates the leading-order result of Ref. [64] to include the $1/m_b$ correction, which turns out to be simply the additional multiplicative factor $(f_{B^*}/f_B)^{-1}$ in the soft-pion limit. In Fig. 25 we plot the ratio of $(f_0/f_+)/(1 - q^2/M_{B^*}^2)$ obtained using the coefficients of our preferred z expansion in Table XIV. We also show the theoretical expectation from Eq. (5.22), taking the HPQCD Collaboration's recent three-flavor lattice-QCD result for the decay-constant ratio $f_{B^*}/f_B = 0.941(26)$ [65], and using the same value of $g_{B^* B \pi} = 0.45(8)$ as in our chiral-continuum extrapolation. The large width of the expected band is due to the

generous range taken for $g_{B^* B \pi}$. Higher-order corrections in the heavy-quark expansion are expected to be small. Taking a conservative value for $\Lambda = 500$ MeV and $m_b = 4.2$ GeV, one would estimate $(\Lambda/m_b)^2$ corrections to be about 1%. The difference of f_{B^*}/f_B from 1 also provides a measure of $\Lambda/m_b \sim 6\%$, which would indicate that $(\Lambda/m_b)^2$ corrections may even be below the percent level. The lattice form factors agree with the theoretical expectation for $q^2 \gtrsim 27$ GeV^2.

D. Determination of $|V_{ub}|$

We now combine our lattice form factors with experimental data for $B \to \pi \ell \nu$ to obtain $|V_{ub}|$. The Standard
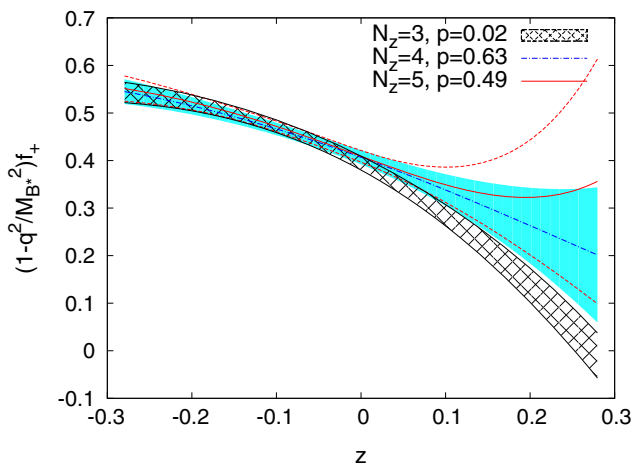
FIG. 22 (color online). Effects of truncating the z expansion for f_+. The areas indicated by the hatched band, colored shaded band, and the lines are results with 1σ errors for $N_z = 3, 4, 5$ z fits, respectively.

TABLE XIII. Results of simultaneous fits of f_+ and f_0 with the kinematic constraint. The $N_z = 4$ fit is our preferred result.

| Fit	$N_z = 3$	$N_z = 4$	$N_z = 5$
$\chi^2/\text{d.o.f.}$	2.5	0.64	0.73
d.o.f.	6	4	2
p	0.02	0.63	0.48
$\sum B_{mn}^+ b_m^+ b_n^+$	0.11(2)	0.016(5)	1.0(2.3)
$\sum B_{mn}^0 b_m^0 b_n^0$	0.33(8)	2.8(1.7)	8(19)
$f(0)$	0.00(4)	0.20(14)	0.36(27)
b_0^+	0.395(15)	0.407(15)	0.408(15)
b_1^+	−0.93(11)	−0.65(16)	−0.60(21)
b_2^+	−1.6(1)	−0.5(9)	−0.2(1.4)
b_3^+		0.4(1.3)	3(4)
b_4^+			5(5)
b_0^0	0.515(19)	0.507(22)	0.511(24)
b_1^0	−1.84(10)	−1.77(18)	−1.69(22)
b_2^0	−0.14(25)	1.3(8)	2(1)
b_3^0		4(1)	7(5)
b_4^0			3(9)
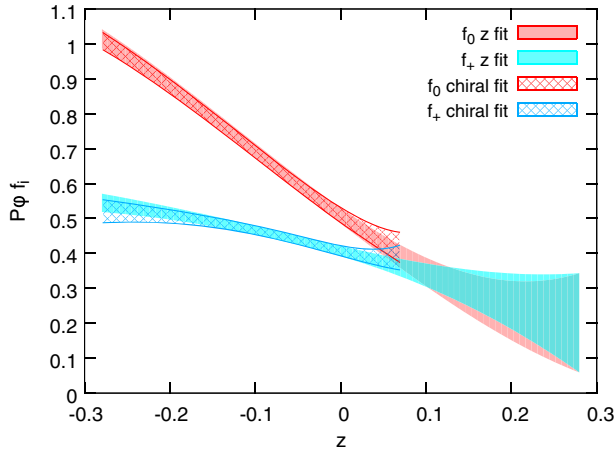
FIG. 23 (color online). z-fit results for the form factors f_0 and f_+ as functions of z.

Model partial branching fraction is $\tau_B d\Gamma/dq^2$, where $d\Gamma/dq^2$ is defined in Eq. (1.1). The contribution from f_0 is negligible due to the small lepton mass. Given $f_+(q^2)$, the branching fraction in the ith q^2 bin $[q_i^2, q_{i+1}^2]$ is

$$\Delta\mathcal{B}_i^{\text{fit}} = C_B^2 |V_{ub}|^2 \int_{q_i^2}^{q_{i+1}^2} |\boldsymbol{p}_\pi(q^2)|^3 |f_+(q^2)|^2 dq^2, \quad (5.23)$$

where $C_B^2 = (\tau_B G_F^2)/(24\pi^3)$ is a constant. For the combined lattice plus experiment z fit, we define a χ^2 for the experimental measurements $\Delta\mathcal{B}_i^{\text{exp}}$ as

$$\chi_{\text{exp}}^2 = \sum_{i,j} (\Delta\mathcal{B}_i^{\text{exp}} - \Delta\mathcal{B}_i^{\text{fit}}) \text{Cov}_{ij}^{\text{exp}} (\Delta\mathcal{B}_j^{\text{exp}} - \Delta\mathcal{B}_j^{\text{fit}}), \quad (5.24)$$

where $\Delta\mathcal{B}_i^{\text{exp}}$ is the experimentally measured branching fraction in the ith q^2 bin (i is a shorthand notation for each bin in each experiment included in the fit) and Cov^{exp} is the experimental covariance matrix, including the statistical and all systematic errors.

We use the experimental results compiled by the Heavy Flavor Averaging Group (HFAG) [6]: BABAR untagged

6-bin analysis (2011) [7], Belle untagged 13-bin analysis (2011) [9], BABAR untagged 12-bin analysis (2012) [8], and Belle tagged analysis with 13 bins for the B^0 and 7 bins for the B^- mode (2013) [10]. For convenience in the fit, we assume isospin symmetry to convert the Belle tagged B^- data to the B^0 mode via

$$\Delta\mathcal{B}(B^0 \to \pi^+ \ell^- \nu)_{\text{Belle},B^-} = 2\frac{\tau_{B^0}}{\tau_{B^-}} \Delta\mathcal{B}(B^- \to \pi^0 \ell^- \nu), \quad (5.25)$$

where $\tau_{B^0} = 1.519(7)$ ps and $\tau_{B^-} = 1.641(8)$ ps are from the PDG [66].

We omit systematic correlations between the BABAR and Belle analyses, because they do not share any major systematic errors. The BABAR 6-bin and 12-bin data have very small overlaps in the selection of samples, so the statistical errors can be considered approximately uncorrelated. There is some systematic correlation between the two analyses, which is, however, supposed to be insignificant [67]. The Belle untagged and tagged data are also largely uncorrelated because the dominant source of systematic errors in these two measurements are very different. In summary, we take the four experimental analyses as independent measurements.

On the other hand, there are systematic correlations between the two isospin modes of the Belle tagged data, which we estimate as follows: Let $\Delta\mathcal{B}_i^-$ and $\Delta\mathcal{B}_\alpha^0$ be the branching fractions in the ith and αth bin of the charged and neutral decay modes, respectively. Let σ_x^-, σ_x^0 be the systematic uncertainties of the two modes from source x, and let r_x^{-0} be the correlation between them. Then we estimate the off-block-diagonal elements of the systematic error covariance matrix by

$$S_{i\alpha} = \sum_{x \in \text{all sys}} r_x^{-0} (\sigma_x^- \sigma_x^0 \Delta\mathcal{B}_i^- \Delta\mathcal{B}_\alpha^0), \quad (5.26)$$

where the sum is over all sources of systematic errors. That said, only a few of the systematic errors contribute

TABLE XIV. Central values, errors, and correlation matrix of the coefficients of f_+ and f_0 from the $N_z = 4$ lattice-only z fit with the kinematic constraint.

|	b_0^+	b_1^+	b_2^+	b_3^+	b_0^0	b_1^0	b_2^0	b_3^0
	0.407(15)	−0.65(16)	−0.46(88)	0.4(1.3)	0.507(22)	−1.77(18)	1.27(81)	4.2(1.4)
b_0^+	1	0.451	0.161	0.102	0.331	0.346	0.292	0.216
b_1^+		1	0.757	0.665	0.430	0.817	0.854	0.699
b_2^+			1	0.988	0.482	0.847	0.951	0.795
b_3^+				1	0.484	0.833	0.913	0.714
b_0^0					1	0.447	0.359	0.189
b_1^0						1	0.827	0.500
b_2^0							1	0.838
b_3^0								1
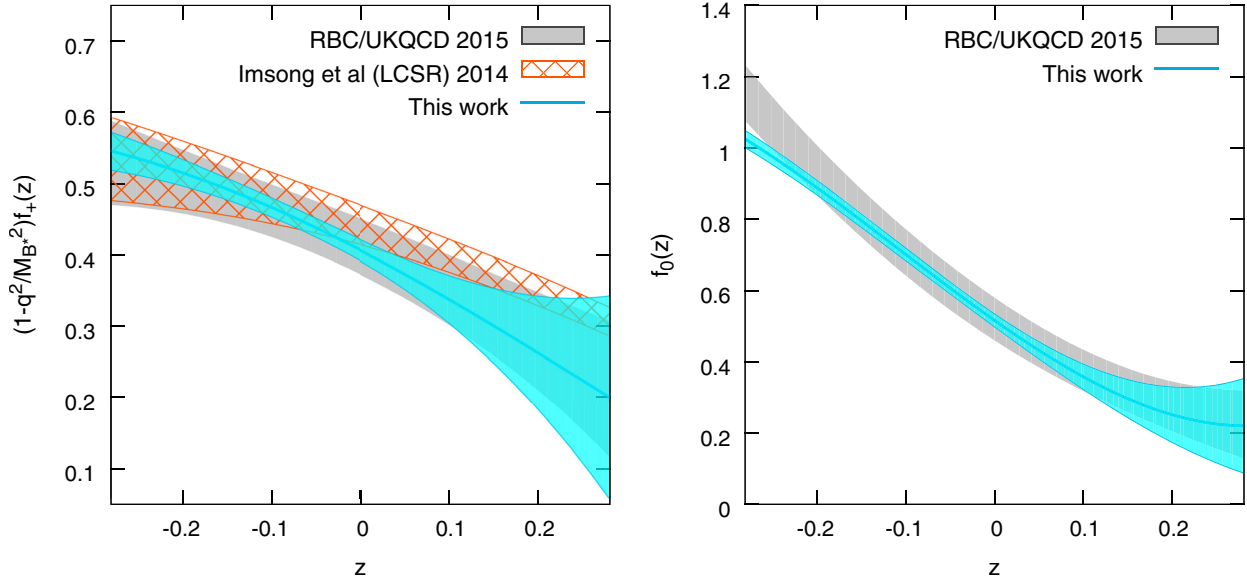
FIG. 24 (color online).   Comparison of f_+ (left) and f_0 (right) from the z-expansion fit results of this work with recent theoretical calculations using light-cone sum rules (LCSR) [62] and lattice QCD [13].

noticeably to the sum, and the biggest source of error, the tag calibration, dominates. From the correlation matrices, we construct the total covariance matrices of each isospin decay mode by adding the statistical matrices and the systematic matrices. We then take the direct sum of the covariance matrices of the B^- and B^0 modes block-diagonally and add the off-block-diagonal elements $S_{i\alpha}$ so that we can fit them simultaneously.

We first fit the z expansion to the experimental data only and without any constraints on the coefficients. We use the BCL formula with three parameters, $N_z = 3$, where the

normalization is $|V_{ub}|b_0$. The result is shown in Table XV. To check the consistency in the shape among the experimental data sets, we also fit each experimental data set separately. The individual fits all have acceptable confidence levels and p values, but the combination of all four data sets gives a rather poor fit that is not improved by going to higher order in z, e.g., $N_z = 4$. The poor fit stems from the *BABAR*11 measurement, which is only marginally consistent with the other three. Figure 26 compares the
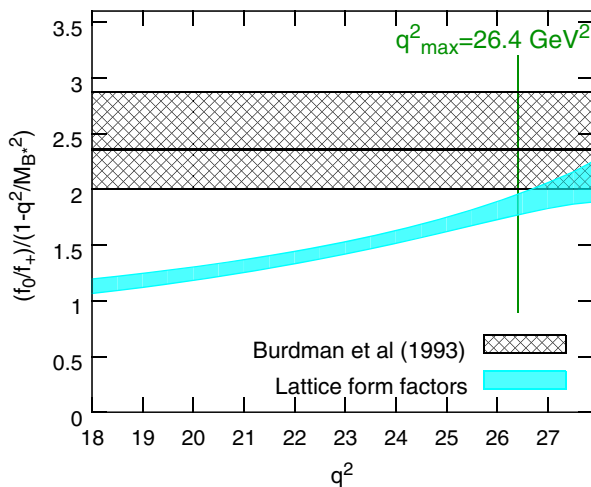
FIG. 25 (color online).   The lattice form-factor ratio $(f_0/f_+)/(1 - q^2/M_{B^*}^2)$ versus q^2 (cyan shaded band) compared with the prediction in the soft-pion limit from heavy-quark symmetry and χPT [63] (hatched band). The width of the hatched band reflects only the uncertainty from $g_{B^*B\pi} = 0.45(8)$ and not other theoretical errors.
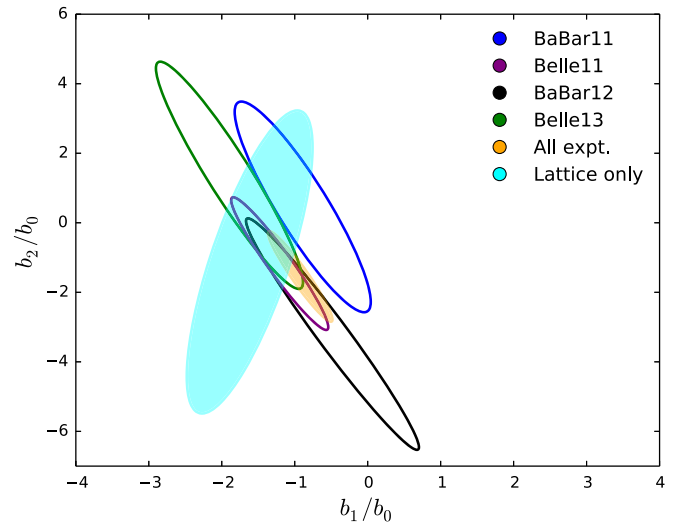
FIG. 26 (color online).   The contour plot of the slope b_1/b_0 and curvature b_2/b_0 of the form factor f_+. The open ellipses are the 1σ contour of the slope and curvature constructed from the three-parameter z fit to individual experimental data. The gold-filled ellipse is from the combined fit of all experimental data. The cyan-filled ellipse is from the four-parameter z fit to lattice form factors.

TABLE XV. The results of fits to experimental data only.

Fit	χ^2/d.o.f.	d.o.f.	p	b_1/b_0	b_2/b_0	$b_0|V_{ub}| \times 10^{-3}$
All exp.	1.5	48	0.02	−0.93(22)	−1.54(65)	1.53(4)
BABAR11 [7]	2	3	0.12	−0.89(47)	0.5(1.5)	1.36(7)
BABAR12 [8]	1.2	9	0.31	−0.48(59)	−3.2(1.7)	1.54(9)
Belle11 [9]	1.1	10	0.36	−1.21(33)	−1.18(95)	1.63(7)
Belle13 [10]	1.2	17	0.23	−1.89(50)	1.4(1.6)	1.56(8)

TABLE XVI. Results of the combined lattice + experiment fits with $N_z = 4$.

Fit	χ^2/d.o.f.	d.o.f.	p value	b_0^+	b_1^+	b_2^+	b_3^+	$|V_{ub}|(\times 10^3)$
Lattice + exp (all)	1.4	54	0.02	0.419(13)	−0.495(55)	−0.43(14)	0.22(31)	3.72(16)
Lattice + BABAR11 [7]	1.1	9	0.38	0.414(14)	−0.488(73)	−0.24(22)	1.33(44)	3.36(21)
Lattice + BABAR12 [8]	1.1	15	0.34	0.415(14)	−0.551(72)	−0.45(18)	0.27(41)	3.97(22)
Lattice + Belle11 [9]	0.9	16	0.55	0.412(13)	−0.574(65)	−0.40(16)	0.38(36)	4.03(21)
Lattice + Belle13 [10]	1.0	23	0.42	0.406(14)	−0.623(73)	−0.13(22)	0.92(45)	3.81(25)

shapes (slopes b_1/b_0 and curvatures b_2/b_0) of the separate and combined experimental fits with the lattice-only fit. The lattice form factor shape is consistent with all of the experimental results.

To perform a combined fit to the lattice and experimental data, we define the total chi-squared function,

$$\chi^2 = \chi^2_{\text{lat}} + \chi^2_{BABAR11} + \chi^2_{\text{Belle11}} + \chi^2_{BABAR12} + \chi^2_{\text{Belle13}},$$

$$(5.27)$$

where the lattice and experimental chi-squared functions are defined in Eqs. (5.15) and (5.24), respectively. The fit is

TABLE XVII. The contribution to the total χ^2 from each data set of the combined fit. The column "# data" gives the number of independent functions (for lattice QCD) or the number of bins (for experiment). The total $\chi^2/(\#\text{data})$ agrees with the χ^2/d.o.f. in Table XVI, once the constraint and number of fit parameters have been taken into account.

Data set	# data	χ^2	χ^2/data
Lattice	11	4.8	0.44
BABAR11 [7]	6	20.9	3.5
BABAR12 [8]	12	15.1	1.3
Belle11 [9]	13	13.8	1.1
Belle13 [10]	20	23.5	1.2
Total	62	78.2	1.26

performed to these five independent data sets with common shape parameters b_m and overall normalization $|V_{ub}|$ by minimizing Eq. (5.27). Table XVI summarizes the various fit results. Due to the tension between the experimental data sets, the p value of the fit to the lattice result and all experiments is only 0.02. Table XVII shows the contributions to the total χ^2 from each data set of the combined fit. By far the largest contribution to χ^2/d.o.f. is from the BABAR 6-bin data set, similar to what we find for the experiment-only fits presented in Table XV.

In the combined fit to lattice form factors and experimental data, the kinematic constraint between f_+ and f_0 at $q^2 = 0$ is unimportant for the determination of $|V_{ub}|$. This is because the experimental data constrain the shape at low q^2. Removing the kinematic constraint from the combined fit and fitting only with the vector form factor f_+ changes neither the coefficients of the z expansion nor the value of $|V_{ub}|$. We also try varying the number of parameters b_m in the z expansion (N_z). The results are shown in Table XVIII. Compared to our preferred fit with $N_z = 4$, the fit using $N_z = 3$ gives a very low p value and a shift of about 1σ in both the form factor and $|V_{ub}|$, while the fit result using $N_z = 5$ nearly coincides with that of the $N_z = 4$ fit, and the values of $|V_{ub}|$ are almost identical.

The experimental data are plotted in Fig. 27 (left) along with the z fits to the lattice data and to all experimental data. The lattice form factor and experimental measurements provide complementary information and, when combined,

TABLE XVIII. Combined lattice + experiments z fits with $N_z = 3$, 4, and 5.

N_z	χ^2/d.o.f.	d.o.f.	p value	b_0^+	b_1^+	b_2^+	b_3^+	b_4^+	$|V_{ub}|$
3	2.5	56	0.0	0.425(12)	−0.424(31)	−0.59(9)			3.63(11)
4	1.4	54	0.02	0.419(13)	−0.495(55)	−0.43(14)	0.22(31)		3.72(16)
5	1.5	52	0.01	0.418(13)	−0.491(56)	−0.31(30)	0.01(55)	−0.6(1.9)	3.72(16)
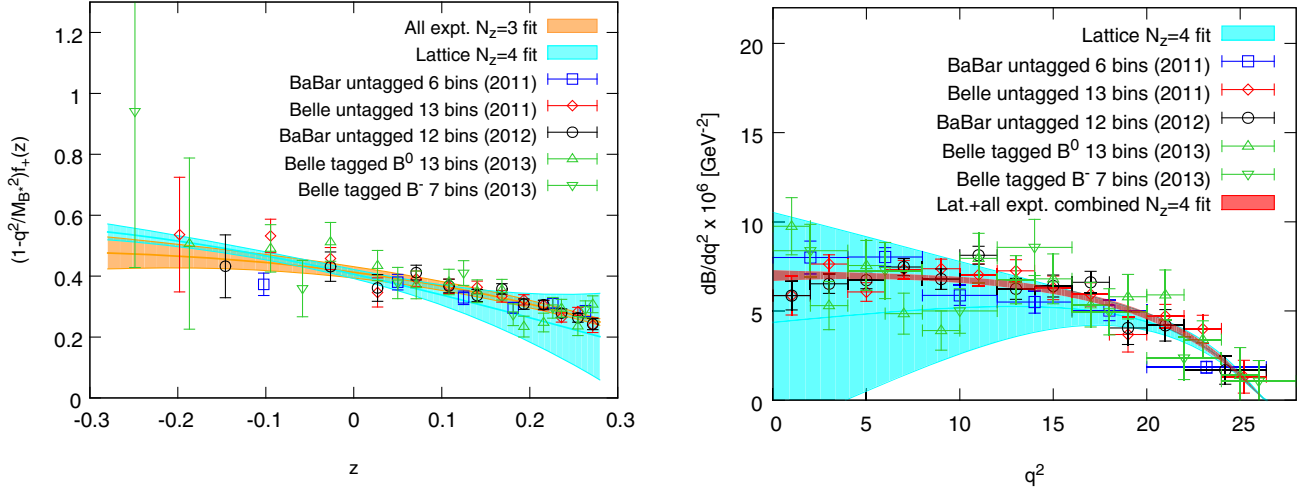
FIG. 27 (color online).   Left: Comparison of vector form factor $f_+(z)$ from z expansion fits to only the lattice-QCD data (cyan band), and to only experimental data including all four measurements (gold band). Right: The similar plot for the partial branching fraction dB/dq^2. The fits including lattice results use $N_z = 4$, while the experiment-only fit uses $N_z = 3$. The experimental data points and the experiment-only z-fit result in the left plot have been converted from $(\Delta\mathcal{B}/\Delta q^2)^{1/2}$ to f_+ using $|V_{ub}|$ from the combined fit. The lattice-only fit result (cyan band) and the combined-fit result (red band) in the right plot are converted from the form factor with the same $|V_{ub}|$.

yield an accurate description of the form factor over the full-q^2 range and hence a precise determination of $|V_{ub}|$. The plot shows that the experimental data dominate the determination of the form-factor shape in the large-z (small-q^2) region while the lattice-QCD form factor dominates the small-z (large-q^2) region. In the intermediate region around $q^2 \sim 20$ GeV^2 ($z \sim 0$), the lattice-QCD and experimental uncertainties are similar in size. This region is decisive in determining $|V_{ub}|$ and, hence, can be used to estimate the separate contributions from lattice and experimental data to the $|V_{ub}|$ uncertainty. At $q^2 = 20$ GeV^2, the error on the lattice-QCD form factor f_+ is about 3.4% (see Table X), and the error on $f_+|V_{ub}|$ from the experiment-only fit is 2.8% at the same momentum. Adding these two errors in quadrature gives a total uncertainty of 4.4%, which is consistent with the error on $|V_{ub}|$ obtained from the full fit, 4.3%. Another estimate of the individual error contribution to $|V_{ub}|$ can be obtained from the uncertainty on the fit parameters from the separate lattice-QCD and experiment fits. From the fit to all experimental data in Table XV, the normalization is $|V_{ub}|b_0 = (1.53 \pm 0.04) \times 10^{-3}$. Similarly, the lattice-only z fit gives the normalization $b_0 = 0.407 \pm 0.015$. Assuming no correlation, one would obtain $|V_{ub}| = (3.76 \pm 0.17) \times 10^{-3}$, which is close to what we obtain from the combined fit.

VI. RESULTS AND CONCLUSION

Our final result for $|V_{ub}|$, obtained from our preferred z fit combining our lattice-QCD calculation of the $B \to \pi\ell\nu$ form factor with experimental measurements of the corresponding decay rate, is

$$|V_{ub}| = (3.72 \pm 0.16) \times 10^{-3}. \qquad (6.1)$$

The error includes all experimental and lattice-QCD uncertainties. The contribution from lattice QCD to the total error is now comparable to that from experiment. The error reported here, following HFAG [6], does not apply the PDG prescription for discrepant data; that prescription [66] would scale the error by a factor of $\sqrt{\chi^2/\text{d.o.f.}} = 1.2$. As can be seen from Table XVII and Fig. 26, the low fit quality is due to the tension between the *BABAR*11 data set and the others. An inspection of all the experimental data in Fig. 27 shows that the point near $z = -0.1$ in the *BABAR*11 data set is lower than the others and a bit more precise than one might have anticipated, but does not suggest that this or any of the data sets have any systematic problems.

We compare our determination of $|V_{ub}|$ with other results in Fig. 28. In particular, our result is consistent with the recent determination from HFAG using our collaboration's 2008 form-factor determination [5] obtained from a small subset of the gauge-field ensembles used in this work. The difference in the central values is due to a small shift in the central values for the form factor f_+ of this analysis compared to our previous analysis [5]. As shown in Fig. 18 (left), the form factor f_+ from this analysis is consistent within errors with the previous analysis, but shifted slightly downward and with an error smaller by roughly a factor of 3. The two analyses have very little statistical and systematic correlation. Our result is also compatible with Standard Model expectations from CKM unitarity [70,71]. Although our determination of $|V_{ub}|$ is higher than that in Ref. [5], and thus closer to the determination from inclusive $B \to X_u$ semileptonic decays
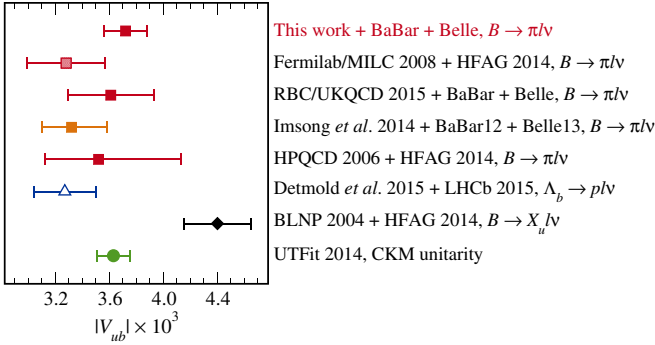
FIG. 28 (color online). Determinations of $|V_{ub}|$. The squares are obtained from $B \to \pi\ell\nu$ decay using theoretical form factors from this analysis, our earlier work [5] (now superseded, but with updated experimental input from HFAG 2014 [6]), a three-flavor lattice calculation by RBC/UKQCD [13], light-cone sum rules (orange square) [62], and HPQCD [4] (using the $q^2 > 16 \text{ GeV}^2$ experimental data only). The blue upward-pointing triangle is obtained from $\Lambda_b \to p\ell\nu$ decay using lattice-QCD form factors from Ref. [68] and experimental data from LHCb [69]. The black diamond shows the inclusive determination using $B \to X_u\ell\nu$ decays [6] with the theoretical approach of Ref. [15]. Also shown is the expectation from CKM unitarity [70] (green-filled circle). For the exclusive determinations from $B \to \pi\ell\nu$ decay (squares), all four experimental results [7–10] are used, except in the LCSR z fit, where only the more recent *BABAR* [8] and Belle [10] data are used.

[6], the inclusive-exclusive disagreement is still greater than 2σ.

A byproduct of the combined lattice and experiment fit is a more precise determination of the vector and scalar form

factors than from the lattice-QCD calculation alone. Both form factors f_+ and f_0 are well determined from lattice QCD in the high-q^2 region, and f_+ is strongly constrained by experiment in the low-q^2 region. This information is then transferred to f_0 via the kinematic constraint $f_0(0) = f_+(0)$. The resulting form factors are shown in Fig. 29. The corresponding z-expansion coefficients and their correlations are given in Table XIX. These represent the present best knowledge of the $B \to \pi\ell\nu$ form factors, and can be used in other phenomenological applications or to test other nonperturbative QCD calculations.

Future improvements in the determination of the $B \to \pi$ semileptonic form factor f_+ will further reduce the uncertainty on $|V_{ub}|$. If the uncertainty of $f_+^{B\to\pi\ell\nu}$ at $q^2 \sim 20 \text{ GeV}^2$ can be reduced further from 3.4% to 1.5%, we would expect a precision of 3% in $|V_{ub}|$, using the current experimental input. With the anticipated improvement in the experimental rate measurement from Belle II, this error would be reduced further. The reduction of uncertainty in $f_+^{B\to\pi\ell\nu}$ is expected with the newly available MILC gauge ensembles that are being generated using the highly improved staggered quark (HISQ) action [72]. The new HISQ ensembles have statistics similar to the asqtad ensembles, but with much smaller light-quark discretization effects. Further, the HISQ ensembles simulated at the physical light-quark masses will remove the need for a chiral extrapolation, thereby eliminating a significant source of uncertainty in this work. These ensembles have already helped to determine the form factor $f_+^{K\to\pi\ell\nu}(0)$ [73] and the leptonic decay constants $f_{D_{(s)}}$ and f_K [74], and hence the relevant CKM matrix elements $|V_{us}|$, $|V_{cd}|$, and
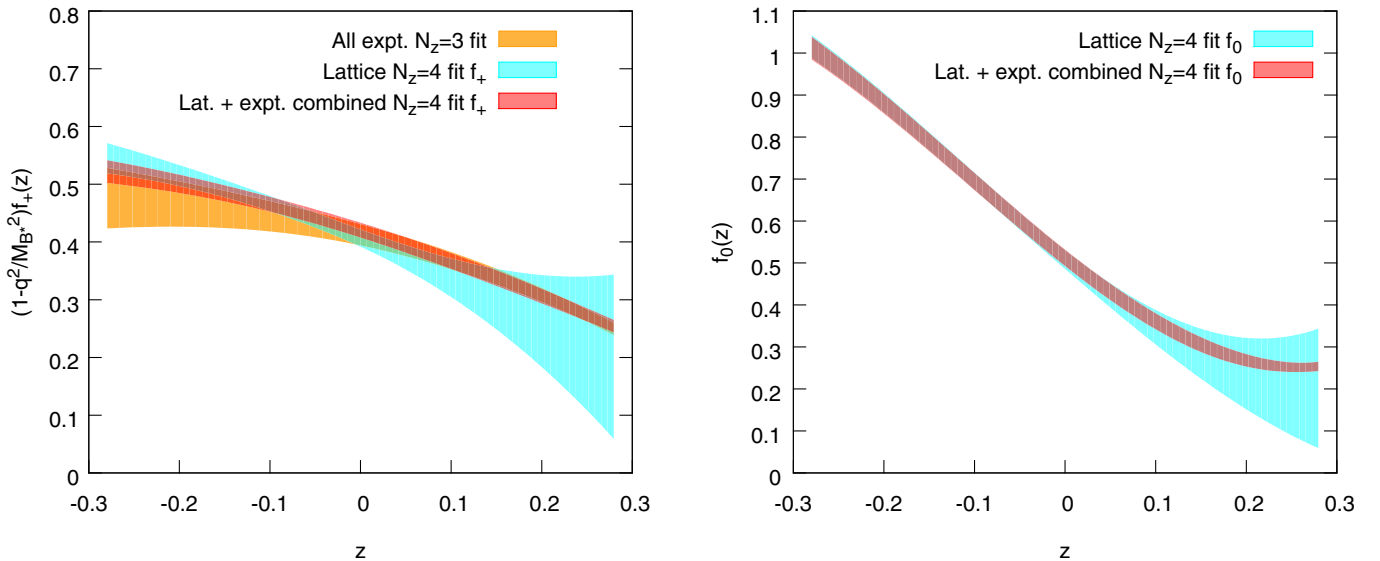

FIG. 29 (color online). The form factors $f_+(z)$ (left) and $f_0(z)$ (right) from the z fits to the lattice data (cyan band), to all experiments (gold band), and to the lattice data plus experiments (red band). The fits including lattice results use $N_z = 4$ and the kinematic constraint, while the experiment-only z fit uses $N_z = 3$. The experiment-only z-fit result has been converted from $(\Delta\mathcal{B}/\Delta q^2)^{1/2}$ to f_+ using $|V_{ub}|$ from the combined fit.

TABLE XIX. Central values, errors, and correlation matrix of the coefficients of f_+ and f_0 from the $N_z = 4$ z fit combining lattice and all four experiments.

	$\|V_{ub}\| \times 10^3$	b_0^+	b_1^+	b_2^+	b_3^+	b_0^0	b_1^0	b_2^0	b_3^0
	3.72(16)	0.419(13)	−0.495(54)	−0.43(13)	0.22(31)	0.510(19)	−1.700(82)	1.53(19)	4.52(83)
$\|V_{ub}\|$	1	−0.870	−0.400	0.453	0.428	−0.175	−0.201	−0.119	−0.009
b_0^+		1	0.140	−0.455	−0.342	0.224	0.174	0.047	−0.033
b_1^+			1	−0.789	−0.874	−0.068	0.142	0.025	−0.007
b_2^+				1	0.879	−0.051	−0.253	0.098	0.234
b_3^+					1	0.076	0.038	0.018	−0.200
b_0^0						1	−0.043	−0.604	−0.388
b_1^0							1	−0.408	−0.758
b_2^0								1	0.457
b_3^0									1

$|V_{cs}|$, with high precision. All of these improvements will further refine and reduce the uncertainties in $|V_{ub}|$, and may also help to resolve the inclusive/exclusive puzzle.

[1] N. Cabibbo, Unitary Symmetry and Leptonic Decays, Phys. Rev. Lett. **10,** 531 (1963).

[2] M. Kobayashi and T. Maskawa, *CP* violation in the renormalizable theory of weak interaction, Prog. Theor. Phys. **49,** 652 (1973).

[3] A. Crivellin and S. Pokorski, Can the Differences in the Determinations of V_{ub} and V_{cb} Be Explained by New Physics? Phys. Rev. Lett. **114,** 011802 (2015).

[4] E. Dalgic, A. Gray, M. Wingate, C. T. H. Davies, G. P. Lepage, and J. Shigemitsu (HPQCD Collaboration),

B meson semileptonic form-factors from unquenched lattice QCD, Phys. Rev. D **73**, 074502 (2006); **75**, 119906(E) (2007).

[5] J. A. Bailey *et al.* (Fermilab Lattice and MILC Collaborations), The $B \to \pi \ell \nu$ semileptonic form factor from three-flavor lattice QCD: A model-independent determination of $|V_{ub}|$, Phys. Rev. D **79**, 054507 (2009).

[6] Y. Amhis *et al.* (Heavy Flavor Averaging Group), Averages of B-Hadron, C-Hadron, and tau-lepton properties as of early 2012, arXiv:1207.1158; updated results as of summer 2014 on the website http://www.slac.stanford.edu/xorg/hfag/.

[7] P. del Amo Sanchez *et al.* (*BABAR* Collaboration), Study of $B \to \pi \ell \nu$ and $B \to \rho \ell \nu$ decays and determination of $|V_{ub}|$, Phys. Rev. D **83**, 032007 (2011).

[8] J. P. Lees *et al.* (*BABAR* Collaboration), Branching fraction and form-factor shape measurements of exclusive charmless semileptonic B decays, and determination of $|V_{ub}|$, Phys. Rev. D **86**, 092004 (2012).

[9] H. Ha *et al.* (Belle Collaboration), Measurement of the decay $B^0 \to \pi^- \ell^+ \nu$ and determination of $|V_{ub}|$, Phys. Rev. D **83**, 071101 (2011).

[10] A. Sibidanov *et al.* (Belle Collaboration), Study of exclusive $B \to X_u \ell \nu$ decays and extraction of $\|V_{ub}\|$ using full reconstruction tagging at the Belle experiment, Phys. Rev. D **88**, 032005 (2013).

[11] V. G. Lüth, Semileptonic B decays, arXiv:1209.4674.

[12] F. Bahr *et al.* (ALPHA Collaboration), $|V_{ub}|$ determination in lattice QCD, *Proc. Sci.*, ICHEP2012 (2013) 424.

[13] J. M. Flynn, T. Izubuchi, T. Kawanai, C. Lehner, A. Soni, R. S. Van de Water, and O. Witzel, The $B \to \pi \ell \nu$ and $B_s \to K \ell \nu$ form factors and $|V_{ub}|$ from $2 + 1$-flavor lattice QCD with domain-wall light quarks and relativistic heavy quarks, Phys. Rev. D **91**, 074510 (2015).

[14] C. M. Bouchard, G. P. Lepage, C. J. Monahan, H. Na, and J. Shigemitsu (HPQCD Collaboration), B and B_s semileptonic decay form factors with NRQCD/HISQ quarks, *Proc. Sci.*, LATTICE2013 (2014) 387.

[15] S. W. Bosch, B. O. Lange, M. Neubert, and G. Paz, Proposal for a Precision Measurement of $|V_{ub}|$, Phys. Rev. Lett. **93**, 221801 (2004).

[16] D. Du, J. A. Bailey, A. Bazavov, C. Bernard, A. X. El-Khadra, S. Gottlieb, R. D. Jain, and A. S. Kronfeld *et al.*, $B \to \pi \ell \nu$ and $B \to \pi \ell^+ \ell^-$ semileptonic form factors from unquenched lattice QCD, *Proc. Sci.*, LATTICE2013 (2014) 383.

[17] J. A. Bailey *et al.* (Fermilab Lattice and MILC Collaborations), $B \to \pi \ell \nu$ semileptonic form factors from unquenched lattice QCD and determination of $|V_{ub}|$, *Proc. Sci.*, LATTICE2014 (2014) 385.

[18] A. X. El-Khadra, A. S. Kronfeld, P. B. Mackenzie, S. M. Ryan, and J. N. Simone, The semileptonic decays $B \to \pi$ lepton neutrino and $D \to \pi$ lepton neutrino from lattice QCD, Phys. Rev. D **64**, 014502 (2001).

[19] A. Bazavov *et al.*, Nonperturbative QCD simulations with $2 + 1$ flavors of improved staggered quarks, Rev. Mod. Phys. **82**, 1349 (2010).

[20] C. W. Bernard, T. Burch, K. Orginos, D. Toussaint, T. A. DeGrand, C. E. Detar, S. Datta, S. A. Gottlieb, U. M. Heller,

and R. Sugar, The QCD spectrum with three quark flavors, Phys. Rev. D **64**, 054506 (2001).

[21] C. Aubin, C. Bernard, C. DeTar, J. Osborn, S. Gottlieb, E. B. Gregory, D. Toussaint, U. M. Heller, J. E. Hetrick, and R. Sugar, Light hadrons with improved staggered quarks: Approaching the continuum limit, Phys. Rev. D **70**, 094505 (2004).

[22] P. Weisz, Continuum limit improved lattice action for pure Yang-Mills theory: 1, Nucl. Phys. **B212**, 1 (1983).

[23] P. Weisz and R. Wohlert, Continuum limit improved lattice action for pure Yang-Mills theory: 2, Nucl. Phys. **B236**, 397 (1984); **B247**, 544(E) (1984).

[24] M. Lüscher and P. Weisz, On-shell improved lattice gauge theories, Commun. Math. Phys. **97**, 59 (1985); **98**, 433(E) (1985).

[25] T. Blum, C. DeTar, S. Gottlieb, K. Rummukainen, U. M. Heller, J. E. Hetrick, D. Toussaint, R. L. Sugar, and M. Wingate (MILC Collaboration), Improving flavor symmetry in the Kogut-Susskind hadron spectrum, Phys. Rev. D **55**, R1133 (1997).

[26] G. P. Lepage, Flavor symmetry restoration and Symanzik improvement for staggered quarks, Phys. Rev. D **59**, 074502 (1999).

[27] J. F. Lagae and D. K. Sinclair, Improved staggered quark actions with reduced flavor symmetry violations for lattice QCD, Phys. Rev. D **59**, 014511 (1998).

[28] K. Orginos, and D. Toussaint (MILC Collaboration), Testing improved actions for dynamical Kogut-Susskind quarks, Phys. Rev. D **59**, 014501 (1998).

[29] K. Orginos, D. Toussaint, and R. L. Sugar (MILC Collaboration), Variants of fattening and flavor symmetry restoration, Phys. Rev. D **60**, 054503 (1999).

[30] C. W. Bernard, T. Burch, T. A. DeGrand, C. DeTar, S. Gottlieb, U. M. Heller, J. E. Hetrick, K. Orginos, B. Sugar, and D. Toussaint (MILC Collaboration), Scaling tests of the improved Kogut-Susskind quark action, Phys. Rev. D **61**, 111502 (2000).

[31] A. X. El-Khadra, A. S. Kronfeld, and P. B. Mackenzie, Massive fermions in lattice gauge theory, Phys. Rev. D **55**, 3933 (1997).

[32] B. Sheikholeslami and R. Wohlert, Improved continuum limit lattice action for QCD with Wilson fermions, Nucl. Phys. **B259**, 572 (1985).

[33] C. W. Bernard, T. Burch, K. Orginos, D. Toussaint, T. A. DeGrand, C. DeTar, S. Gottlieb, U. M. Heller, J. E. Hetrick, and B. Sugar (MILC Collaboration), The static quark potential in three flavor QCD, Phys. Rev. D **62**, 034503 (2000).

[34] R. Sommer, A New way to set the energy scale in lattice gauge theories and its applications to the static force and alpha-s in SU(2) Yang-Mills theory, Nucl. Phys. **B411**, 839 (1994).

[35] A. Bazavov *et al.* (MILC Collaboration), MILC results for light pseudoscalars, *Proc. Sci.*, CD09 (2009) 007.

[36] C. T. H. Davies, E. Follana, I. D. Kendall, G. Peter Lepage, and C. McNeile (HPQCD Collaboration), Precise determination of the lattice spacing in full lattice QCD, Phys. Rev. D **81**, 034506 (2010).

[37] A. Bazavov *et al.* (Fermilab Lattice and MILC Collaborations), B- and D-meson decay constants from three-flavor lattice QCD, Phys. Rev. D **85,** 114506 (2012).

[38] R. Arthur *et al.* (RBC and UKQCD Collaborations), Domain wall QCD with near-physical pions, Phys. Rev. D **87,** 094514 (2013).

[39] D. P. Menscher, Ph.D. thesis, University of Illinois, 2005.

[40] M. Wingate, J. Shigemitsu, C. T. H. Davies, G. P. Lepage, and H. D. Trottier, Heavy light mesons with staggered light quarks, Phys. Rev. D **67,** 054505 (2003).

[41] A. S. Kronfeld, Application of heavy quark effective theory to lattice QCD: 1. Power corrections, Phys. Rev. D **62,** 014505 (2000).

[42] J. Harada, S. Hashimoto, K. I. Ishikawa, A. S. Kronfeld, T. Onogi, and N. Yamada, Application of heavy quark effective theory to lattice QCD: 2. Radiative corrections to heavy light currents, Phys. Rev. D **65,** 094513 (2002); **71,** 019903(E) (2005).

[43] G. P. Lepage and P. B. Mackenzie, On the viability of lattice perturbation theory, Phys. Rev. D **48,** 2250 (1993).

[44] J. A. Bailey *et al.* (Fermilab Lattice and MILC Collaborations), Update of $|V_{cb}|$ from the $\bar{B} \to D^* \ell \bar{\nu}$ form factor at zero recoil with three-flavor lattice QCD, Phys. Rev. D **89,** 114504 (2014).

[45] Ran Zhou *et al.* (to be published).

[46] C. Aubin and C. Bernard, Heavy-light semileptonic decays in staggered chiral perturbation theory, Phys. Rev. D **76,** 014002 (2007).

[47] C. Aubin and C. Bernard, Staggered chiral perturbation theory for heavy-light mesons, Phys. Rev. D **73,** 014515 (2006).

[48] W. Detmold, C.-J. D. Lin, and S. Meinel, Axial Couplings and Strong Decay Widths of Heavy Hadrons, Phys. Rev. Lett. **108,** 172003 (2012).

[49] W. Detmold, C. J. D. Lin, and S. Meinel, Calculation of the heavy-hadron axial couplings g_1, g_2, and g_3 using lattice QCD, Phys. Rev. D **85,** 114508 (2012).

[50] J. M. Flynn, P. Fritzsch, T. Kawanai, C. Lehner, C. T. Sachrajda, B. Samways, R. S. Van de Water, and O. Witzel, The $B^*B\pi$ coupling with relativistic heavy quarks, *Proc. Sci.*, LATTICE2013 (2014) 408.

[51] J. Bulava *et al.* (ALPHA Collaboration), The $B^*B\pi$ coupling in the static limit, *Proc. Sci.*, LATTICE2010 (2010) 303.

[52] D. Becirevic, S. Prelovsek, and J. Zupan, $B \to \pi$ and $B \to K$ transitions in partially quenched chiral perturbation theory, Phys. Rev. D **68,** 074003 (2003).

[53] D. Becirevic, S. Fajfer, and J. F. Kamenik, Use and misuse of ChPT in the heavy-light systems, *Proc. Sci.*, LAT2007 (2007) 063.

[54] J. Bijnens and I. Jemos, Hard pion chiral perturbation theory for $B \to \pi$ and $D \to \pi$ form factors, Nucl. Phys. **B840,** 54 (2010); **B844,** 182(E) (2011).

[55] G. Colangelo, M. Procura, L. Rothen, R. Stucki, and J. Tarrus Castella, On the factorization of chiral logarithms in the pion form factors, J. High Energy Phys. 09 (2012) 081.

[56] H. Na, C. T. H. Davies, E. Follana, G. P. Lepage, and J. Shigemitsu (HPQCD Collaboration), $|V_{cd}|$ from D meson leptonic decays, Phys. Rev. D **86,** 054510 (2012).

[57] C. G. Boyd and M. J. Savage, Analyticity, shapes of semileptonic form-factors, and anti-$B \to \pi$ lepton anti-neutrino, Phys. Rev. D **56,** 303 (1997).

[58] C. G. Boyd, B. Grinstein, and R. F. Lebed, Constraints on Form-Factors for Exclusive Semileptonic Heavy to Light Meson Decays, Phys. Rev. Lett. **74,** 4603 (1995).

[59] C. Bourrely, I. Caprini, and L. Lellouch, Model-independent description of $B \to \pi l \nu$ decays and a determination of $|V_{ub}|$, Phys. Rev. D **79,** 013008 (2009); **82,** 099902(E) (2010).

[60] J. Mercer, Functions of positive and negative type, and their connection with the theory of integral equations, Phil. Trans. R. Soc. Ser. A **209,** 415 (1909).

[61] T. Becher and R. J. Hill, Comment on form-factor shape and extraction of $|V_{ub}|$ from $B \to \pi l \nu$, Phys. Lett. B **633,** 61 (2006).

[62] I. S. Imsong, A. Khodjamirian, T. Mannel, and D. van Dyk, Extrapolation and unitarity bounds for the $B \to \pi$ form factor, J. High Energy Phys. 02 (2015) 126.

[63] G. Burdman, Z. Ligeti, M. Neubert, and Y. Nir, The decay $B \to \pi$ lepton neutrino in heavy quark effective theory, Phys. Rev. D **49,** 2331 (1994).

[64] M. B. Wise, Chiral perturbation theory for hadrons containing a heavy quark, Phys. Rev. D **45,** R2188 (1992).

[65] B. Colquhoun, C. T. H. Davies, R. J. Dowdall, J. Kettle, J. Koponen, G. P. Lepage, and A. T. Lytle, B-meson decay constants: A more complete picture from full lattice QCD, arXiv:1503.05762.

[66] K. A. Olive *et al.* (Particle Data Group), Review of particle physics, Chin. Phys. C **38,** 090001 (2014).

[67] J. Dingfelder (private communication).

[68] W. Detmold, C. Lehner, and S. Meinel, $\Lambda_b \to p \ell^- \bar{\nu}_\ell$ and $\Lambda_b \to \Lambda_c \ell^- \bar{\nu}_\ell$ form factors from lattice QCD with relativistic heavy quarks, arXiv:1503.01421.

[69] R. Aaij *et al.* (LHCb Collaboration), Determination of the quark coupling strength $|V_{ub}|$ using baryonic decays, arXiv:1504.01568.

[70] M. Bona *et al.* (UTfit Collaboration), The unitarity triangle fit in the Standard Model and hadronic parameters from lattice QCD: A reappraisal after the measurements of $\Delta m(s)$ and BR($B \to \tau\nu(\tau)$), J. High Energy Phys. 10 (2006) 081; updated results as of summer 2014 on the website http://www.utfit.org.

[71] J. Laiho, E. Lunghi, and R. S. Van de Water, Lattice QCD inputs to the CKM unitarity triangle analysis, Phys. Rev. D **81,** 034503 (2010).

[72] A. Bazavov *et al.* (MILC Collaboration), Lattice QCD ensembles with four flavors of highly improved staggered quarks, Phys. Rev. D **87,** 054505 (2013).

[73] A. Bazavov *et al.* (Fermilab Lattice and MILC Collaborations), Determination of $|V_{us}|$ from a Lattice-QCD Calculation of the $K \to \pi \ell \nu$ Semileptonic Form Factor with Physical Quark Masses, Phys. Rev. Lett. **112,** 112001 (2014).

[74] A. Bazavov *et al.* (Fermilab Lattice and MILC Collaborations), Charmed and light pseudoscalar meson decay constants from four-flavor lattice QCD with physical light quarks, Phys. Rev. D **90,** 074509 (2014).